FUNCTIONALIZED ELECTROSPUN SCAFFOLD AS DRESSING FOR SKIN AND BONE REPAIR

HO PAN BEI

MPhil

The Hong Kong Polytechnic University

2021

The Hong Kong Polytechnic University

Department of Biomedical Engineering

Functionalized Electrospun Scaffold as Dressing for Skin and Bone Repair

Ho Pan Bei

A thesis submitted in partial fulfillment of the requirements for the degree of Master of Philosophy

July 2021

Certificate of Originality

I hereby declare that this thesis is my own work and that, to the best of my knowledge and belief, it reproduces no material previously published or written, nor material that has been accepted for the award of any other degree or diploma, except where due acknowledgement has been made in the text.

_____

BEI Ho Pan

Abstract

Electrospinning is an advanced technique for creation of nanofibrous structures. Its versatility and flexibility to create varied nanofibers and scaffolds enabled fabrication of biomimetic structures. Of note, many of the human organs and tissues exhibit nanofibrous architecture owing to the nature of extracellular matrix, which consists of fibrils of nanoscale that encourage cell adhesion. Thus, many studies have been inspired by this happy coincidence and fully utilized electrospinning for creating artificial tissues such as skin, periosteum and neural sheaths. The use of nanofibers for tissue engineering have proved to become extremely beneficial both bench side and clinical owing to its unique capabilities to support cell growth and provide a platform for localized release of therapeutics. However, existing techniques leave much to be desired: The inherently low drug diffusion distance causes fast leakage of encapsulated therapeutics; The use of natural polymers in electrospinning favours cell adhesion and biocompatibility, but lacks long-term stability or drug release owing to the hydrolysis of polymer chains. Additionally, their lack of intrinsic strength causes them to rupture easily under external stress, which limits their sites of application. Here we introduce two novel studies to improve on existing electrospinning technology for the creation of artificial skin for prevention of hypertrophic scar, and the synthesis of reinforced natural polymer artificial periosteum for bone regeneration.

Hypertrophic scarring has no definitive known cause, but afflicts millions of patients worldwide. Current understanding of scar pathophysiology mainly attributes it to the occurrence of inflammation and disruptions in intrinsic signaling of fibroblasts which cause them to overproliferate and form fibrous tissues. To address the clinical issue, invasive techniques such as injection of inhibitory drugs and surgical excision have been employed with limited success. Notably, the lack of sustained supply of fibroblast inhibitors lead to high recurrence rate of scar

formation. Here, we employed a core-sheath electrospun fibrous scaffold encapsulating polymer brush grafted mesoporous silica nanoparticles for delivery of anti-scarring agents. The scaffold demonstrates sustained release of small molecules over 90 days, and successfully inhibited the proliferation of fibroblasts without significantly impeding cell adhesion. Rabbit ear hypertrophic scar model also well demonstrated the clinical relevancy of the anti-scarring fibrous scaffold through reduction in scar thickness and reduced collagen deposition in low dosage groups, indicating the success of this long-term drug delivery strategy.

The periosteum is a dense, fibrous structure covering the surface of bones and rich with architectures that recruit osteoblasts and endothelial cells. Studies have proven that the periosteum exhibits strong osteogenesis and angiogenesis during bone regeneration, and that the damaged tissues lead to slow recovery or incomplete healing. Studies in the past have fabricated fibrous artificial periosteum with osteogenic-angiogenic coupling, but their mechanical properties are lacking and cannot resemble the toughness of native periosteum. Here we employed a natural polymer/artificial polymer network alongside organic/inorganic crosslinking network with acrylate group functionalized hydroxyapatite nanoparticles and ionic interactions with L-arginine for the fabrication of a robust, nanofibrous periosteum with high bioactivity and release of therapeutics to stimulate the NO/cGMP pathway for the simultaneous promotion of osteogenesis and angiogenesis. The addition of various components into the system greatly enhanced GelMA's inherent low strength, and imbued it with osteogenic and angiogenic properties. The scaffold exhibited good biocompatibility for both MSCs and HUVECs, and was able to induce bone formation and vessel formation in each cell types respectively.

Acknowledgements

First of all, I would like to give my sincerest gratitude to my supervisor, Dr. Xin Zhao for her support and guidance. Her encouragements and advice to put me on the right track is invaluable during my research. Her enthusiasm in research also inspires students with new ideas, and would discuss them extensively with students to spark new projects. This will no doubt make a significant impact in my future career, and to one day, lead a team of my own.

Then I would like to thank Dr. Yu Tian, who had responsibly introduced me to lab practice and conducting experiments. Under his leadership I was able to quickly grasp the basics of using lab equipment and gain independence. I would like to thank Mr. Chun Hei Lam, Roy for his continuous support with cell culture experiments, as well as purchasing of lab reagents. Only with his excellent management am I able to conduct experiments without worry and smoothly finish my lab duties.

I would also like to thank all of our group members, Dr. Yuhe Yang, Qiang Zhang, Quanjing Mei, Mengna Zhao, Jingdong Rao, Di Suo, Tianpeng Xu, Bo Liang, Huaqian Liu, Ho Yin Yuen for the assistance with lab work as well as constructive comments during my 2 years' MPhil study. I would also like to thank my friends Lejian Liu, Yu Kun Lam, Chi Hin Hung for their friendship and company during both the happy and dark times.

Last but not least, I would like to dedicate my gratitude to my parents for their everlasting love and support, and their encouragements for me continue my postgraduate studies.

Table of Contents

List of Figures

Chapter 1 Introduction

1.1 History and mechanics of electrospinning

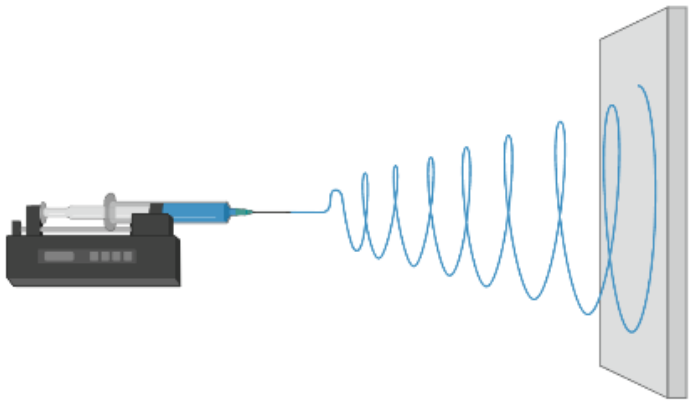

Figure 1. Schematic depicting a typical electrospinning set-up.

Electrospinning is a bottom-up fabrication technique to create nano-sized (1-1000 nm) fibers in diameter. The term “electrospinning” is crowned owing to its utilization of strong electrical potential to create jets of polymer fibers, or in laymen terms, elongated, threadlike structures that are 1 dimensional[1]. The formation of nanoscale fibers relies on the slow feeding of polymer solution and formation of Taylor Cone at the needle tip, which is a unique structure where sessile polymer solution charged with electrical potential forms a cone where the apex emits an extremely thin line of polymer solution to be deposited on the grounded receiver[2]. The diameter of electrospun fibers can be modulated through various parameters including solution feed speed, voltage, distance between needle tip and collector, as well as some external factors such as humidity and temperature[3]. Rigorous requirements are needed when deciding on the polymer solution for electrospinning as shear thinning is an important component for the successful spinning[4]. When the solution is either too viscous or too thin, shear thinning would not be able to occur and instead droplets will be dispensed from the needle tip, which is often referred to as electrospraying. On the other hand, the solvent of the solution needs to meet certain criteria as well, including its boiling point, polarity and solubility of the substrate[5]. A low boiling point allows for quick evaporation of the solvent from the polymer jet, ensuring the formation of solid fibers on the collector to avoid inter-linkage between each individual fibers or merging of fibers into one bulk structure. The polarity of the spinning solvent promotes the electrical expulsion of polymer solution, increasing the effectiveness of the voltage provided. The solvent also needs to fully dissolve the substrate as incomplete dissolution of the polymer in the solution may cause instability in the formation of Taylor Cone, as well as clogging of the needle tip during the lengthy spinning process.

Many studies have attempted to optimize the spinning parameters to create structures beneficial to their respective applications. Notably, electrospinning was chosen as the fabrication technique owing to its ability to generate nanoscale fibers of a reasonable quantity to create tissue scaffolds. While electrospinning is a small-scale process and cannot be simply upscaled through the increase in polymer feed speed as the spinning solution surface tension is finite, its versatility and simplicity in the synthesis process of nanofibrous scaffolds attracted the attention of many tissue engineers. Notably, the structural merits of electrospun fibers reside in its nanoscale morphology, which resembles the fibrous tendrils of the natural extracellular matrix (ECM). Studies have shown that cells are more prone to adhering to surfaces that are uneven, and the woven nanofibrous structure provides a site for anchoring and can promote cell attachment, proliferation and migration[6]. Cells such as fibroblasts were demonstrated to secrete increased collagen 1 and retain their phenotypic morphology according to the nanofiber alignment, which promotes their bioactivity. Interestingly, the ability for cells to adhere to the nanofibrous scaffold surface can be manipulated by tuning the printing parameter of the collector. For instance, a rotating disk collector was demonstrated to create fibers of good alignment, and neural stem cells seeded onto the fibrous scaffold demonstrated elongation and neurite outgrowth in perfect parallel to the fiber aligned direction[7]. This opens up many opportunities for engineering electrospun scaffolds towards directing cell fate.

Other structures of electrospinning include mixing nanoparticles in the polymer solution for formation of nano fibers with solute scattered lumen, emulsion nanofibers which include tiny pores of separate phase solution within the fibers, and core-sheath nano fibers which incorporates a continuous phase of core fluid separated from its shell within the fiber lumen[8]. These structures are often used for encapsulation of suitable reagents for tissue engineering purposes. For example, core-sheath nanofibers are used for long-term drug delivery owing to its increased diffusion distance from the core phase to the external environment. However, the initial burst release is almost unavoidable as the influx of aqueous fluids causes a change in pressure which causes potential cracks and ruptures on the fiber surface. On the other hand, the outer surface of electrospun fibers can be chemically functionalized with active molecules such as targeting agents for increased recruitment of cells or responsive ligands that react to changes to the external environment to achieve triggered drug release[9, 10].

1.2 Electrospinning skin scaffolds for cutaneous regeneration

1.2.1 Structure of human skin and pathophysiology of hypertrophic scarring

As the largest organ in the body, the human skin is a complex, multilayered structure with unique properties such as protection from external pathogens, modulation of water loss and provides a large reservoir of extracellular matrix for cell-cell interactions[11]. The most outer layer, the epidermis, consists of mostly dead keratinocytes which shields the interior from damage, invasion of pathogens, and radical changes in temperatures. The inner layer is the dermis, which are the layer that are prone to scarring when damaged[12]. The dermis is an integrated system of extracellular matrix with many cell types including fibroblasts, mast cells and macrophages. The dermis is a key player in wound healing and remodeling. This layer also contains the blood vessels, lymphatic systems and neural networks. Lastly, the subcutaneous layer provides cushioning and contains adipose tissues, which serves as an energy reserve for the body.

After suffering an injury, the cutaneous wound goes through a lengthy wound healing cycle in order to restore the tissue morphology and functions to before trauma. The process lasts for around 90 days in total and is critical to the formation of hypertrophic scars. The hemostasis phase lasts for mere minutes where blood clot is formed at the open wound. The enzyme thrombin activates blood platelets and initiates the formation of a fibrin mesh, which stabilizes the clumped platelets into a blood clot. This serves as a coagulation process to stem the continuous bleeding and loss of body fluids. The inflammatory phase focuses on the removal of debris and destruction of pathogens that have entered the wound. This phase lasts for four to six days and involves the recruitment of neutrophils and macrophages to clear debris, secrete growth factors for activation of the immune system, as well as reddening and heating up of the surrounding area to promote cell activity to facilitate wound repair. The proliferative phase focuses on filling out the empty wound with connective tissues, endothelialization and recruitment of body cells to the injury site. It lasts for 4 to 24 days. The maturation phase slowly reorganizes the collagen fibers and matures the newly formed tissue to regain tensile strength (80% of per-injured strength), and is most prone to disruptions owing to systemic and local factors, which leads to scarring. This can last from 21 days to around 2 years, though the general consensus on the wound healing cycle typically ranges from 2 to 3 months.

There are numerous contributing factors to pathological scarring. Thankfully, the advancement in biological assay technology has shed a new light on the cause of scar formation and strategies to combat the clinical issue. TGF-β is a family of growth factors widely believed to contribute towards fibroblast activity[13]. Studies revealed that fibroblasts extracted from hypertrophic scars exhibited different phenotypes compared with normal scar tissues or healthy skin. Interestingly, pathological fibroblasts expressed both upregulated and prolonged expression of TGF-β, and that the persistence of this phenomenon may cause a positive feedback loop which results in the fibrotic phenotype. Targeting the same pathway, many studies have attempted the knockdown of Smad, which inhibits the downstream TGF-β activity and promotes wound

healing. On the other hand, inflammatory genes were demonstrated to alter the outcome of wound healing. In particular, IL-6 and IL-37 are emerging cytokines that modulate immune responses, and were observed to have increased secretion in keloid tissues. On the other hand, areas of high tension or frequent movements were shown to contribute towards scarring. The cyclical stretch potentially upregulates the expression of genes and growth factors, as well as matrix remodeling but down regulates the apoptotic genes, which possibly contributes towards the uncontrolled proliferation of fibroblasts at the wound bed. Additionally, stretching was shown to increase the number of myofibroblasts recruited to the wound, while reduction in tension was demonstrated to reduce the incidence of scarring in clinical cases[14]. These all offer great insight to devising strategies for the treatment of cutaneous/burn wounds and prevention of scar formation.

1.2.2 Current progress on treatment of hypertrophic scarring

Current clinical treatment strategies include intralesional injections, cryotherapy, surgical manipulation, and laser therapy[15]. The latter three can be considered surgical procedures to remove fibrotic tissues, and are invasive techniques that may cause tissue necrosis post-surgery, blistering and pain. The injection of anti-scarring agents, however, is the gold standard for current treatment of hypertrophic scars, involving the weekly or biweekly injection directly into the scar tissues. However, the frequent injections are inconvenient to patients, and without a localized release, diffused drugs may cause side effects to the surrounding tissues. Over the years, many researchers started devised strategies to achieve drug release with wound dressings encapsulating a variety of drugs, including small molecules, siRNAs and growth factors due to their fast application and approximation to the trauma site[16]. Existing wound dressings include hydrocolloids, hydrogels, silicone films and dry gauze. However, the limited extracellular matrix (ECM)-mimetic structure of these wound dressings limits their ability to support wound closure.

While important breakthroughs on scar formation cellular pathways have been made due to rigorous study of interference drugs' effect on fibroblast activity, most studies pan for no more than a week due to the quick release of therapeutics[17, 18]. Notably, the traditional skin patch approach release the encapsulated drugs in mere hours, while gels applied directly to wound sites degrade quickly and releases all the content in a matter of days[19]. More success was observed in sutures, where drug molecules were incorporated directly within the solid fiber lumen[20]. Yet sutures dispense all drugs when immersed in fluids within a week. On the other hand, a newly developed approach to wound treatment is the artificial skin, which includes many commercially available products such as Integra, Alloderm and Biobrane. These usually contain components of the ECM such as collagen and is focused on accelerating the repair of patient skin after trauma such as large area burn wounds. In many clinical studies, artificial skin was shown to significantly lower the length of stay of severely injured patients [21]. However, their frequent replacement and high biodegradability make them unsuitable for long-term drug delivery.

Electrospinning was chosen by many researchers to synthesize wound dressings due to its ease of handling to create cell-adhesive nanofibers[22]. As a technique it has been widely utilized and researched for fabrication of membranes not only in the biomedical field, but in industry and textile. Nano sized fibers are favourable for wound healing due to its high resemblance to the native ECM environment, which allows for improved cell adhesion and proliferation[23]. The wide range of materials that can be electrospun also opens up many opportunities for functional materials. Natural materials favourable for wound healing such as gelatin could be electrospun with the right solvent to create niche micro-environments[24]. This soft aqueous material has been shown to accelerate wound healing and reduce scarring by many studies, but has low bulk mechanical properties similar to hydrogels of the same family. Hyaluronic acid, aloe vera gel and glucomannan all share the same weakness as gelatin while promoting wound healing, but gelatin has been shown to possess the highest spinnability out of all aqueous biopolymers, being able to

be spun without heat or blending with synthetic polymers. On the other hand, synthetic polymers such as polycaprolactone (PCL), polylactic acid (PLA) and polyethylene glycol (PEG) have received equal attention in electrospinning owing to their improved shear thinning ability and mechanical strength compared with natural polymers. To compensate for their lack of bioactive molecules for adhesion, various techniques were employed to coat the surface with proteins and therapeutic molecules to enhance their biocompability and regenerative efficacy[25]. However, surface functionalized molecules quickly detach and degrade under physiological conditions, which limit their long-term effectiveness after implantation.

Better engineered fibers emerged recently to combat the fast diffusion of therapeutics such as core-shell fibers and nanoparticle-encapsulated fibers where drug molecules were incorporated in multilayered lumens[26, 27]. These lengthen the drug release profile to around a month due to the increased drug diffusion route[28]. However, significant initial release continues to be an issue as interference drugs are preferably released at later stages of wound healing. Wound healing lasts for around 90 days, with the remodeling stage starting as late as two weeks after initial trauma. It is preferred to have anti-scarring agents perform staggered release and lasting until wound healing is complete to reduce side effects on healing efficacy and prevent scar formation. While studies have successfully designed scaffolds with triggered release for improved drug release timings, the difference between the presence of stimulus was shown to be small, and the fibers were unable to prevent leakage and retain most of its encapsulated drugs over 20 days at a dormant state[29].

1.3 Electrospinning artificial periosteum for bone regeneration

1.3.1 Structure of periosteum

The periosteum is a tough, fibrous bilayer of tissues that cover the surface of the bone. It has significant contributions to bone growth and repair, with implications for blood supply[30]. Its structure can be classified into an outer and inner layer: The outer layer is an inelastic tissue with small compact bundles of elongated fibroblasts. Its surface architecture attracts endothelial attachment and is the most vascularized substratum of the periosteum, allowing for providing sufficient blood supply to and skeletal muscles. The deeper regions of the outer layer is considered to be more elastic but less vascularized; The inner cambium layer is a dense layer of tissues home to mesenchymal progenitors, osteoblasts and fibroblasts. It also possesses rich vascular and neural networks, which have high osteoblastic potential. As age develops, the cambium becomes thinner and with it a reduction in its osteogenic potential, which explains to reduction in bone quality in senior adults.

After a bone fracture, periosteum is the major player in bone regeneration in the form of endochondral bone repair. Firstly, a hematoma stabilizes the surrounding tissues and would be replaced with a fibrous layer of periosteum. Cells from the cambium are then stimulated to differentiate and proliferate, while membranous ossification is initiated to establish an outline of the new bone formation with the help of vasculature. Then a mass of cartilage is formed by the cambium and ossified to replace the lost tissues. However, this healing mechanic is not present in bones that lack a periosteum. In case of poor vasculature or large bone defects where the periosteum is significantly damaged, endochondral bone repair cannot initiate and instead the defect site would be covered by fibrous tissues called a soft callus.

1.3.2 Current progress on treatment of bone fracture healing

Bones are the backbone of the skeletal system. Owing to their composite structure of both cells and minerals, it provides the human body with shape and mechanical support, alongside protection to interior organs and movement[31]. Additionally, bones were demonstrated to regulate energy metabolism and mineral homeostasis of the body. However, after a fracture, bones face many challenges in its complete recovery. Autografts and allografts are the clinical gold standards for the treatment of bones, but lacks cellular components owing to the removal of cells from the ossified matrix to avoid autoimmune responses. As such fracture sites are prone to nonunion of tissues owing to the lack of vasculature in the grafted implants. For more severe fractures, screws and support is required to maintain the stability of the fracture, and to keep damaged tissues in contact with one another. Yet this also causes additional damage to the healthy bone, which were drilled into by screws and causes debris and damage to the vasculature.

More methods for creating artificial periosteum have been reported over the years. Porcine small intestinal submucosa, cell sheets and cell-free composites were all effective substitutes to the natural periosteum[32]. However, most of them lack the fibrous nature and cell recruitment potential of native periosteum, limiting their clinical efficacy at inducing bone regeneration. Of note, microgrooves on PLGA sheets were able to stimulate cell alignment with high stability, which offers implications for bone graft designs.

Selective gene induction has revealed much of the signaling mechanisms during bone healing. BMP-2, TGF-β are two major pathways in the modulation of osteogenic differentiation of mesenchymal stem cells into osteoblastic cells. The downstream action of BMP-2 is also responsible for the recruitment of progenitor cells as well as the chondro-osteogenesis and ECM synthesis in preparation of ossification. Wnt pathway was also demonstrated to modulate bone repair and skeletal homeostasis, and was applied for the treatment of bone fractures[33]. However, the cascading action of Wnt signaling may cause the development of cancer, in addition to programmed cell death. On the other hand, the NO-cGMP pathway have proved to be a signaling pathway that regulates both osteogenesis and angiogenesis[34, 35]. Nitric oxide is demonstrated to regulate osteoclasts, which are bone-resorption cells, downregulating their activity while upregulating the activity of osteoblasts. Additionally, nitric oxide can stimulate re-endothelialization of endothelial and stem cells, which contributes vascularization in bone healing.

1.3.3 Use of electrospinning on fabrication of artificial periosteum

Many studies have attempted the fabrication of the complex periosteum architecture with electrospun scaffolds owing to its nanofibrous nature. Notably, they are often loaded with therapeutic agents targeting specific pathways for bone regeneration, with biomimetic designs and components designed to improve biocompatibility. Examples include Icariin loaded PCL/gelatin fibers, calcium phosphate/GelMA fibers, Deferoxamine loaded PCL fibers etc.[36-38]. However, these studies were not able to focus on the mechanical properties of the artificial periosteum, which is required to both provide mechanical stability and prevent soft tissue ingrowth. Additionally, they were not able to consider the *in vivo* degradation of the scaffold, leading to short-term therapeutic efficacy by design. Most critically, the vascularization aspect of bone healing was neglected by these studies, which would not be able to support the endochondral bone regeneration and cause further complications. Herein, while numerous studies have attempted to fabricate biomimetic and osteogenic periosteum, their clinical relevancy when applied to actual bone fractures remain questionable.

2. Project aim

The aim of our study is to thus optimize both study designs and electrospinning parameters to fabricate high performance tissue regeneration scaffolds to overcome traditional weaknesses of existing studies. This is performed through careful evaluation of chosen materials, structures and practicability of said scaffolds through thorough consideration of both its working mechanism in theory and potential clinical application in surgical procedure/treatments.

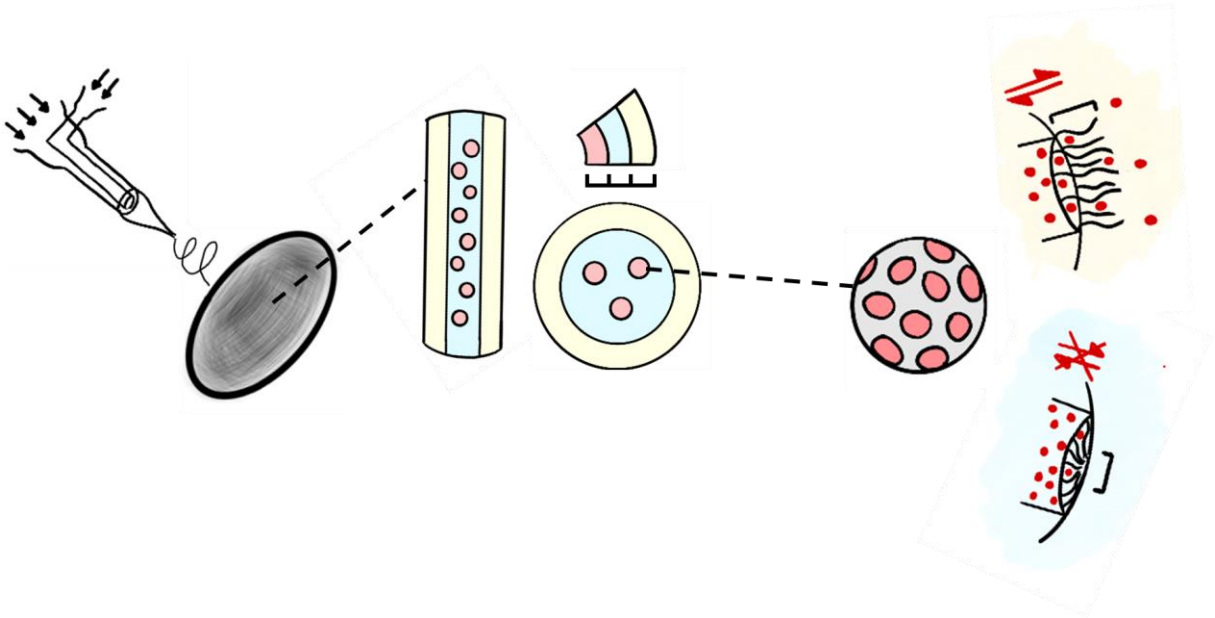

Figure 2. Schematic depicting project outline of long-term drug release from electrospun fibrous scaffolds. Core-sheath fibers are produced using co-axial electrospinning of PLA and MSN embedded ethanol. MSNs are functionalized with PLA brushes and loaded with anti-scarring agents.

For a wound dressing designed for the prevention of hypertrophic scars, we employ a core-sheath electrospinning with nanoparticle encapsulation design. The core sheath spinning will consist of an organic phase as shell and aqueous phase as core, which was demonstrated to increase the drug diffusion distance and extend the release profile of therapeutics loaded in the core[39]. The organic phase will be PLA, as its hydrophobicity can slow down the influx of water while its biodegradability allow for slow degradation of the scaffolds during wound healing[40]. The aqueous phase will consist of ethanol for its lowered surface tension and ability to provide an aqueous, fluidic medium to disperse nanoparticles[41]. This is achieved by emulsion electrospinning to minimize the contact between gated nanoparticles and organic solvents for prevention of drug leakage and burst release. The nanocarriers are mesoporous silica nanoparticles, which demonstrated good drug loading efficiency and were approved by the U.S. Food and Drug Administration. Its pores will be capped by PLA brushes as polymer caps/brushes were widely reported to be effective at modulating responsive drug release[42]. Here, PLA brushes are grafted from the nanopore surface to collapse upon exposure to aqueous environments to slow down the release of anti-scarring agents, while they extend when immersed

in drug loaded organic solvents for encapsulation. This lock-and-key mechanism ensures the high loading capacity of the carriers while reducing the drug leakage it may undergo post-application. The chosen anti-scarring agent is doxorubicin owing to its high solubility in organic solvents and partial solubility in aqueous environments. Its ability to hinder cell proliferation owing to DNA disruption effectively slows down the activity of fibroblasts[43]. It is envisioned that this triple-layered design can gradually release its contents over the course of 90 days to inhibit the activity of surrounding fibroblasts without burst release or induce mass apoptosis to the cell colonies. With its implications to scar prevention, this model delivery system can also be applied to other long-term tissue regeneration such as prevention of tendon adhesion with a change in encapsulated therapeutics.

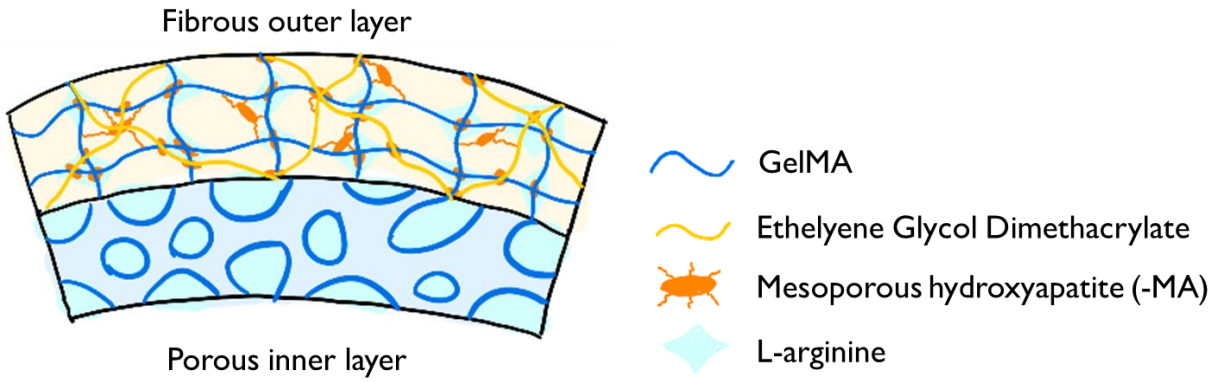

Figure 3. Schematic depicting project outline of organic-inorganic crosslinked periosteum invoking osteogenesis-angiogenesis coupling for large bone repair.

For the spinning of artificial periosteum, mechanical property and bioactivity are the two main design rationales. GelMA will be used for biocompatibility and adhesion to tissues, mixed with ethylene glycol dimethacrylate to improve crosslinking density and slow down degradation[44]. This synthetic/natural polymer network is expected to mimic the elastic/inelastic nature of natural periosteum. To further bolster the bulk strength, mesoporous (Hydroxyethyl) methacrylate-functionalized hydroxyapatite (HA) nanoparticles loaded with L-arginine will be added to the spinning solution to create both an organic/inorganic intercrosslinkable network and ionic bound scaffold. Notably, the Guanidine and α-carboxylic acid groups will interact with Ca^{2+} and PO_4^{3-} respectively to improve its anchoring within HA nanoparticles[45]. This will reinforce the polymer network to produce a mechanically stiff, slow degrading artificial periosteum which has good tissue adhesion properties. Notably, the encapsulated L-arginine serves as a progenitor for nitric oxide (NO) via the NO/cGMP pathway, of which endothelial nitric oxide synthase (eNOS) converts excess L-arginine molecules into NO in a calcium-dependent fashion. NO is a molecule that is responsible for both mediating osteoblastic differentiation as well as vascularization. Its action stimulates the downstream sGC and PKG activity which promotes the differentiation of osteoblastic progenitor cells into osteoblasts, increases their proliferation and improves mineral deposition and bone remodeling[46].

Meanwhile, vascularization differentiation was demonstrated by endothelial cells and HUVECs exposed to increased levels of nitric oxide, which has great implications for restoring the native endochondral bone repair of healthy bone tissues[47]. It is believed that this design allows for this artificial periosteum to be applied in various situations including large bone fracture leading to absence of functional periosteum, as well as in patients with low inherent vascularization efficiency such as diabetic individuals. It is envisioned that this scaffold can be applied efficiently in clinical settings without the aid of external support for stability, and facilitate the fracture healing in terms of both osteogenesis and angiogenesis.

3. Methodology

3.1 Fabrication and characterization of skin scaffold

3.1.1 Synthesis of MSN-NH_2

The MSNs were synthesized using the Stöber method and soft templating. Briefly, 1.82g cetyl trimethyl ammonium bromide (CTAB) were allowed to dissolve in 500 mL deionized water under 80°C. 9 mL tetraethyl orthosilicate (TEOS) was added dropwise into the mixture to react for 1 h. The resulting solution was centrifuged and washed a few times with ethanol and water to remove excess CTAB. The crude product was refluxed in ethanol (250 mL)-HCl (2.5mL) at 80°C for 6 h. The acid-washed MSNs were retrieved by centrifugation and washed with water and ethanol multiple times to remove the remaining CTAB from pores. MSNs were freeze dried to avoid aggregation of particles. They were then added to water/3,3',5,5'-Tetramethylbenzidine (TMB) at 1:1 ratio and allowed to react at 140°C for 24 h to achieve pore enlargement. MSNs were dispersed in 50 mL of anhydrous toluene. 400 μL of (3-Aminopropyl)trimethoxysilane (APTMS) was added slowly into the mixture, and allowed to reflux at 80°C for 6h. The reacted particles were washed with deionized water and ethanol several times and denoted MSN-NH2.

3.1.2 Functionalization of MSNs with PLA using graft-to approach

MSN-NH2s were grafted with PLA brushes using carbodiimide chemistry. Briefly, 100 mg MSN-NH2 was dispersed in 50 mL dichloromethane (DCM) and put under sonication for 2 h. 625 mg PLA, 890 mg dicyclohexylcarbodiimide (DCC) and 260 mg 4-Dimethylaminopyridine (DMAP) were added to 75 mL DCM and sonicated for 2 h. The two mixtures were added together under nitrogen protecting, and sealed into reflux for 6 h at 36°C. The reacted product was centrifuged 3 times and washed with DCM. The nanoparticles were retrieved using soxhlet extraction with hot tetrahydrofuran (THF) at 80°C for 50 h, and denoted as MSN-PLA after drying in vacuo.

3.1.3 Functionalization of MSNs with PLA using graft-from approach

MSN-COOHs were grafted with PLA using “graft from” approach. Briefly, 100 mg MSN-COOH was added to 50 mL flask with 2 g LA monomer and 2.24 μL Tin(II) 2-ethylhexanoate and purged with nitrogen. The system was allowed to react under stirring at 120°C for predetermined intervals. Resultant nanoparticles were washed with chloroform until no trace lactide (LA) or PLA can be detected in the supernatant. Denoted MSN-PLA, they were dried overnight at 60°C.

3.1.4 Characterization of MSNs

Dynamic light scattering (DLS) was performed to determine particle size and zeta potential using water as solvent. Brunauer–Emmett–Teller (BET) analysis was performed to determine surface area and pore size of MSNs. Fourier-transform infrared spectroscopy (FTIR) was performed to

determine the chemical nature of functionalized MSNs. Transmission electron microcopy (TEM) was performed to observe the morphology of MSNs. Thermogravimetric analysis (TGA) from 50°C to 700°C was performed to assess the amount of PLA grafted onto MSN-PLAs.

3.1.5 Electrospinning of core-shell fibers

Hyaluronic acid/PLA fibers were fabricated using emulsion electrospinning. Briefly, 2% HA was dissolved in 3:1 water/DMF solution as the core, and 10% PLA in dichloromethane was used as the shell. Both solutions were mixed until no visible solids are present. Two 10 mL syringes were loaded with respective solutions and connected to a coaxial needle using translucent tubing. The needle was supplied with 20kV voltage using an alligator clamp, whereas the grounded collector was wrapped in aluminum foil and placed 10 cm away from the needle tip. The syringes were then connected to an advancement pump with 0.1 mL/h feed rate. Electrospinning was performed at room temperature for 1 h before the formed membrane on foil was peeled off and allowed to air dry.

Hyaluronic acid (HA)/PLA fibers were fabricated using co-axial electrospinning. Hyaluronic acid was experimented with electrospinning owing to its hydrogel nature as one of the bulk ECM components, and its widely reported effectiveness in skin regeneration. Briefly, 1.5% HA was dissolved in water as the core, and 10% PLA in Hexafluoro-2-propanol (HFIP) was used as the shell. Both solutions were mixed until no visible solids are present. Two 10 mL syringes were loaded with respective solutions and connected to a coaxial needle using translucent tubing. The needle was supplied with 16kV voltage using an alligator clamp, whereas the grounded collector was wrapped in aluminum foil and placed 10 cm away from the needle tip. The syringes were then connected to an advancement pump with 0.6 mL/h feed rate for PLA and 0.1 ml/h for HA. Electrospinning was performed at room temperature for 1 h before the formed membrane on foil was peeled off and allowed to air dry.

Gelatin/PLA fibers were fabricated using co-axial electrospinning. Similar to HA, gelatin as a hydrogel has numerous favourable cell adhesive moieties on its surface, and is commonly used as gel patches for wound healing. Briefly, 35% gelatin was dissolved in glacial acetic acid as the core, and 20% PLA in HFIP was used as the shell. Both solutions were mixed until no visible solids are present. Two 10 mL syringes were loaded with respective solutions and connected to a coaxial needle using translucent tubing. The needle was supplied with 14kV voltage using an alligator clamp, whereas the grounded collector was wrapped in aluminum foil and placed 10 cm away from the needle tip. The syringes were then connected to an advancement pump with 0.2 mL/h feed rate for PLA and 0.1 ml/h for gelatin. Electrospinning was performed at room temperature for 1 h before the formed membrane on foil was peeled off and allowed to air dry.

PVA/PCL fibers were fabricated using co-axial electrospinning. Briefly, 10% PVA and 2% ammonium molybate was dissolved in water as the core, and 30% PCL in was used as the shell. Both solutions were mixed until no visible solids are present. Two 10 mL syringes were loaded

with respective solutions and connected to a coaxial needle using translucent tubing. The needle was supplied with 15kV voltage using an alligator clamp, whereas the grounded collector was wrapped in aluminum foil and placed 10 cm away from the needle tip. The syringes were then connected to an advancement pump with 0.3 mL/h feed rate for PCL and 0.1 ml/h for PVA. Electrospinning was performed at room temperature for 1 h before the formed membrane on foil was peeled off and allowed to air dry.

Ethanol-MSN/PLA fibers were fabricated using coaxial electrospinning. Ethanol was chosen for its shear thinning properties, with minimal impedance to fiber formation compared to highly viscous hydrogels. Briefly, core solution ethanol-MSN and shell solution PLA were prepared as follows: 50 mg/mL MSN was dispersed in ethanol using ultrasound sonication; 20% w/v PLA was added to 10 mL HFIP. Both solutions were mixed until no visible solids are present. Two 10 mL syringes were loaded with respective solutions and connected to a coaxial needle using translucent tubing. The needle was supplied with 10kV voltage using an alligator clamp, whereas the grounded collector was wrapped in aluminum foil and placed 10 cm away from the needle tip. The syringes were then connected to an advancement pump with 1.5 mL/h feed rate for PLA and 0.5 mL/h for ethanol-MSN. Electrospinning was performed at room temperature for 1 h before the formed membrane on foil was peeled off and allowed to air dry.

3.1.6 Characterization of electrospun core-shell membrane

The membranes were characterized using scanning electron microscopy (SEM) and TEM to observe its nanofibrous and core-shell structure.

3.1.7 Loading of MSNs with Dox

50 mg MSNs were added to 50 mg/mL doxrubicin (DOX) HFIP solution and stirred continuously for 24 h. Drug-loaded MSNs were collected by centrifugation, washed thrice with deionized water, dried overnight, and denoted MSN-DOX. MSN-DOXs were dispersed in 2 mL phosphate buffer solution (PBS) in a 2 mL centrifuge tube at pH 7.4, with 1 mL replaced at predetermined intervals. The transferred PBS solution was stored for analysis using visible light-spectrometry at absorbance 480 nm to detect DOX concentration. The loading of MSN-PLA with DOX was performed in same condition.

3.1.8 Characterization of drug release profile

Standard curve of DOX concentration was produced by plotting predetermined concentration of DOX solution in PBS against absorbance, which shows linear relationship. Subsequent DOX solution concentrations were calculated through slope of standard curve. Drug release over time was calculated using equation: Cumulative release = volume of buffer (mL) × drug concentration at time point t + Σ(volume removed × concentration from previous time points), and cumulative percentage was calculated by Cumulative percentage = drug released/drug loaded × 100%. Drug release profiles of MSN and MSN-PLA were assessed in this study.

3.1.9 *In vitro* biocompatibility and proliferation study

Human fibroblasts (3T3s) were used for *in vitro* cell culture. They were cultured in Dulbecco's modified Eagle's medium alpha containing 10% fetal bovine serum. Fibroblasts were incubated at 37°C in a humidified atmosphere of 5% carbon dioxide. 3T3s were passaged using Trypsin/EDTA at 70-80% confluency. For this study, briefly, 3T3 cultures were introduced to MSNs by indirect contact. After incubation with culture medium for 24 h, the Dox-medium is added to 3T3s pre-seeded a day before contact at 2000 cells per well in a 96 well plate. Live-dead assay and CCK-8 assay were used to determine cell density and viability.

3.1.10 *In vivo* wound healing and scar prevention study

In vivo wound healing assay will be performed on cutaneous wound on healthy rabbits. The rabbits will first be sedated and a 6mm-diameter punch will be applied to create spherical biopsies. They will then be divided into control (no treatment), drug (injection of 5-fu), MSN and scaffold group. For non-scaffold groups, the wound will be covered with standard surgical dressing. Photos of wounded area were taken on day 0, 3, 7, 14, with one rabbit sacrificed and scar tissue harvested and stored in 4% paraformaldehyde containing 10% sucrose at 4°C for 12 h and then 30% sucrose for 24 h, and finally embedded in OCT compound and stored at −80°C until analysis. Tissues will be cut at 10 μm, mounted on glass slide and stained with Hematoxylin and eosin stain and Masson’s Trichrome stain for microscopic observation. Wound healing will be assessed by size of wound and histology study of scar tissues, as well as collagen estimation by Masson’s trichrome staining. The scar elevation index is given at height of scar tissue/height of nearby normal tissues while the epidermal thickness index is calculated through height of recovered epidermis/height of healthy skin.

3.1.11 Data processing

Data will be analyzed using SPSS software. Fiber size distribution between different groups will first be analyzed using normality test to ensure normal distribution of fiber diameter within one group. Then the two groups will be compared using two-sample T-test to observe significance in their difference. Linear regression will be performed to assess the reliability of standard calibration curve of Dox concentration against absorbance. Cell number and area will also go through homogeneity of variance test first to ensure normal distribution before comparison using one-way ANOVA to compare significant differences between control, MSN and membrane group. If no normal distribution is observed, non-parametric tests Mann-Whitney U test or Kruskal-wallis test will be performed. For *in vivo* studies, similar analysis methods will be performed on wound size and collagen staining intensity among control, drug, MSN and scaffold groups.

3.2 Fabrication and characterization of periosteum scaffolds

3.2.1 Synthesis of HEMA-functionalized hydroxyapatite nanoparticles

Briefly, 3.408 g Na_2PO_4, 8.74 g CTAB and 2.88g Mesitylene were dissolved in 100 mL deionized water. The pH of this solution is tuned to 10 using 1M sodium hydroxide solution. 5.88 g $CaCl_2$ H_2O is dissolved in 60 mL deionized water, then added dropwise to the other solution. The solution is kept at 80ºC and allowed to react for 24 h before washing with alternating deionized water and ethanol until no emulsion is observed in the supernatant. The formed precipitate was then dried and sintered at 550ºC to remove any excess CTAB and denoted meso HA.

The functionalization of meso HA with HEMA is as follows: 100 mg meso HA was dispersed in 100 mL DMF with 10 mL HMDI and 0.3 mL dibutyl-tin dilaurate and allowed to react for 8 h at 80ºC, before the addition of 8 ml HEMA and further reaction for another 5 h. The resultant particles are washed with DCM for three times and denoted mHAMA. Resultant nHAMAs were characterized using FTIR, BET analysis and TEM imaging.

3.2.2 Electrospinning of GelMA/EGDMA/HAMA-arg scaffolds

10% w/v GelMA is completely dissolved in HFIP to form a consistent polymer solution. For other groups, 1% v/v EGDMA, 0.5% w/v mHAMA and 5/10/20mM L-arginine is added to the spinning solution respectively. The solution is placed in a 10 mL syringe and dispensed at 1 mL/h with a 0.5 mm gauge needle. The connecting voltages are +14-17kV and -2kV for the needle tip and collector. For physical characterization, the electrospinning was allowed to perform for 5 hours while for cell culture experiments, the spinning process lasts for 2 h. The resultant scaffolds were then removed from the collector foil and soaked in 10% w/v Irgacure 2959 with ethanol for 1 h before crosslinked with UV at 365 nm wavelength and 5 mW/cm^2 for 30 minutes per side. The membranes were then washed with ethanol for at least 3 times and immersed in ethanol for storage.

3.2.3 Mechanical testing of GelMA/EGDMA/HAMA-arg scaffolds

Before testing, the scaffolds were immersed in deionized water for 24 h to reach equilibrium. For tensile assessment, after a brief drying to remove excess water, the scaffolds were cut into pieces of 5mm width and fixed onto the Instron mechanical tester using gas-powered clamps. Then the scaffolds were pulled at 10 mm/min and the loading/extension was recorded via the provided software. The Young's modulus is calculated at stress/strain at the tensile region. For burst pressure assessment, 1 cm diameter scaffolds were cut using a hole punch and briefly dried before attachment to a porcine membrane, of which a hole of 2 mm diameter was punctured using a needle. The membrane was then clamped into a gas pressure tester and gas compression was performed by syringe pump. The maximum pressure before scaffold detachment was recorded as burst pressure. For lap shear test, 20% w/v gelatin solution was first applied to the

surface of glass slides as 1 x 1cm squares. After being allowed to dry, scaffolds of the same size were applied on the surface of the gelatin blocks before attaching the glass slides in alternate positions with slight compression. The setup was then tested using Instron mechanical tester at 1mm/min pulling speed. The maximum shear stress was calculated as force/cross-sectional area. 5 replicates were tested per group.

3.2.4 Biocompatibility assessments of GelMA/EGDMA/HAMA-arg scaffolds

MSCs and HUVECs were used as model cells for bone and blood vessels respectively. MSCs were cultured with DMEM while HUVECs were cultured with ECM medium. Both cell types were allowed to grow in cell culture flasks until 70-80% confluence before seeding. To assess viability, 10,000 cells were seeded onto the membranes in 48-well tissue culture plate, stained with Live/Dead staining and performed CCK-8 assay after 1, 3 days. The quantification of living and dead cells was performed by ImageJ from 9 pictures in each group. The quantification of cellular activity was performed using a multimode plate reader at 450 nm absorbance with 4 replicates. To assess the adhesion properties of the scaffolds, 10,000 cells were seeded onto the membranes and stained with Phalloidin 488 and DAPI for the visualization of cytoskeleton and nucleus respectively. Then fluorescence images of cell morphology were observed using a Leica Confocal Microscope.

3.2.5 Nitric oxide production assessment of GelMA/EGDMA/HAMA-arg scaffolds

Briefly, MSCs and HUVECs were seeded onto circular membrane samples respectively at 50,000 cells per cm^2 and allowed to proliferate over 3 days. At the end of the culturing procedure, supernatant culture medium was collected and characterized using a total nitrite assay kit following the instructions of the manufacturer to quantify the amount of dissolved NO.

3.2.6 Osteogenic assessments of GelMA/EGDMA/HAMA-arg scaffolds

MSCs were used as model cells for Alkaline Phosphatase Assay and Alizarin Red S for early and late osteogenic marker assessment respectively. Briefly, cells were seeded onto circular membrane samples at 10000 cells per well (48 well plate), and cultured with osteogenic differentiation medium. After 3 days, samples were stained with ALP assay kit according to manufacturer's instructions, and crystal formation was observed using an optical microscope to determine the degree of osteogenic differentiation. After 7 days, different samples were fixed and stained with ARS assay kit according to manufacturer's instructions and observed using an optical microscope for red colour and precipitate formation to quantify calcium deposits.

3.2.7 Angiogenic assessments of GelMA/EGDMA/HAMA-arg scaffolds

The angiogenic assessment was performed through tube formation assay of HUVECs. Briefly, periosteum samples were placed at the bottom of 48 well plates, then covered with 300 μL of Matrigel. After crosslinking, the gels were then seeded at 50,000 cells per cm^2 for each well and

coated with 300 μL of ECM medium. Then, over 3, 6, 12 h, the tube formation was observed by calcein staining and brightfield imaging for capturing images. Quantification of tube formation was performed through ImageJ software on 5 different images of the same group.

4. Results and Discussion

4.1 Electrospun skin scaffold for long-term drug delivery

4.1.1 Physical and chemical characterization of nanocarrier

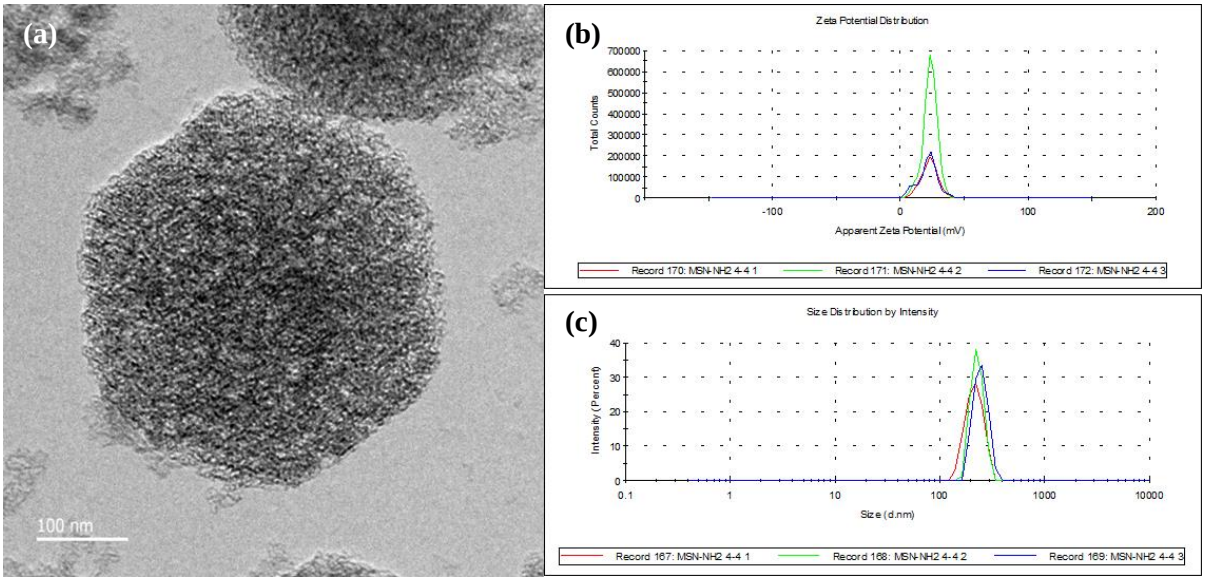

Figure 4. Physical properties of synthesized MSNs. (a) TEM image, (b) Zeta potential and (c) size distribution from DLS analysis.

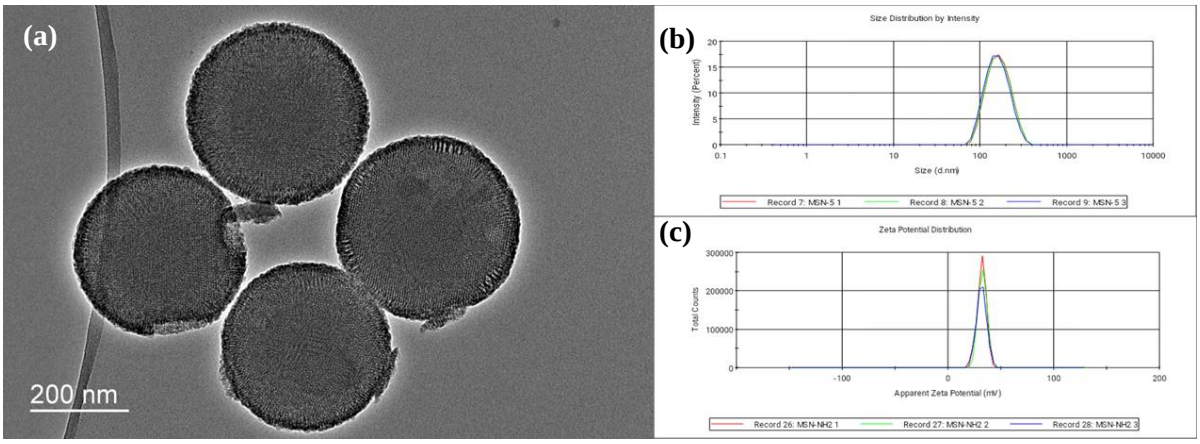

Figure 5. Physical properties of purchased MSNs. (a) TEM image, (b) Zeta potential and (c) size distribution from DLS analysis.

To commence the study, we first need to establish a nanocarrier with good drug loading capacity in preparation for the long-term release. We synthesized MSNs using the Stober soft templating method, and yielded MSNs at around 600 nm size. The surface was then functionalized with amine groups for further reaction. However, we observed that positive zeta potential from DLS was weak, showing a low substitution ratio. Additionally, the uncontrollable mesopore sizes and

morphology may contribute towards inconsistent release kinetics and encapsulation. Due to this, we decided to directly purchase MSNs from Sigma Aldrich, and found that these MSNs have more defined mesoporous structure, are smaller with less diverse sizes, as well as a stronger positive charge. All further MSN samples are thus purchased from Sigma Aldrich for later studies as we are satisfied with these physical properties.

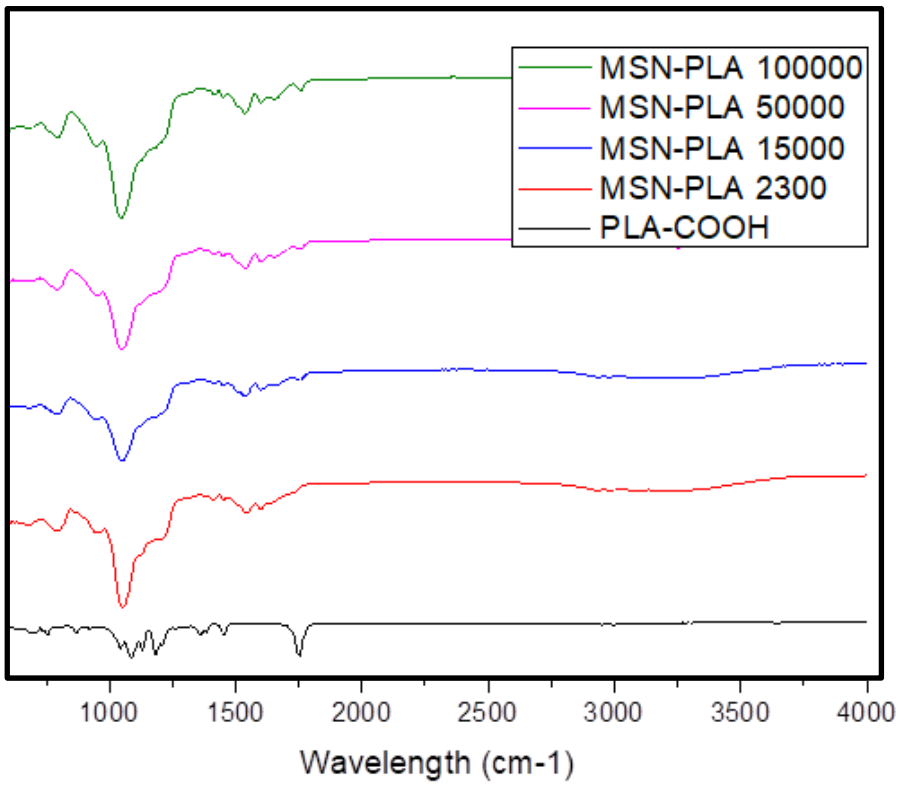

Figure 6. FTIR spectrum of graft to MSN-PLAs with various PLA brush lengths.

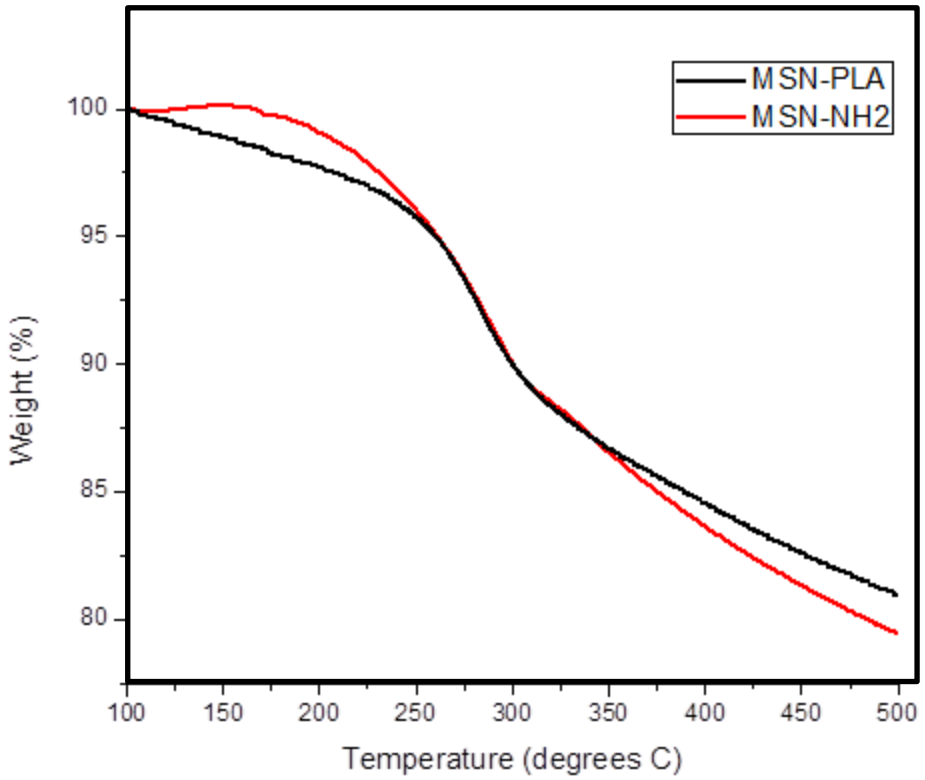

Figure 7. TGA analysis of graft to MSN-PLA and MSN-NH_2.

Graft to is one of the two major functionalization methods for attaching polymer chains onto nanomaterial surface. While it allows for more precise control over the length and nature of the grafted polymer chains, the longer the polymer chain the less reactive and success rate of functionalization becomes[48]. PLA graft to functionalization onto MSN-NH_2 was performed using carbodiimide click-chemistry. However, the C=O peak at 1700 cm^{-1} is very weak for all molecular weight groups, showing unsuccessful functionalization. The small peaks observed possibly result from the incomplete washing of unreacted polymers off the nanoparticle surface. We speculate that this is due to the low reactivity of PLA brushes with only active groups at the end of the polymer. TGA analysis further proves that PLA was not successfully grafted onto as weight loss of both MSN-PLAs and MSNs are not significantly different.

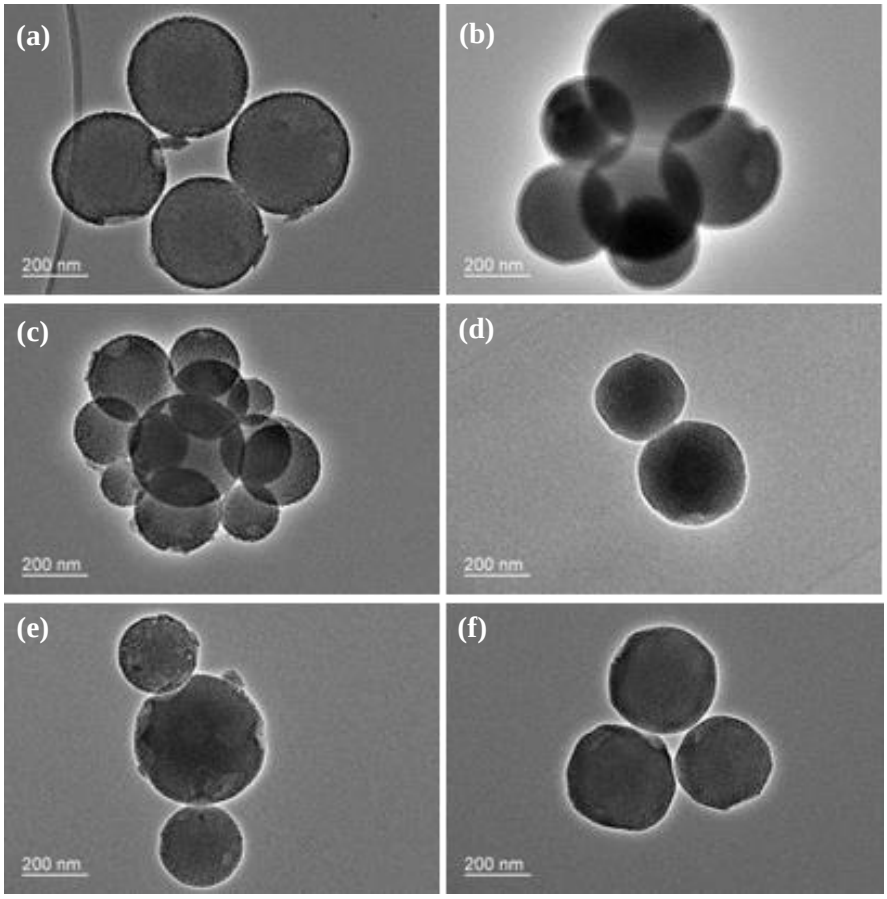

Figure 8. TEM image of graft from (a) MSN-COOH, MSN-PLA- (b) 1 h, (c) 3 h, (d) 6 h, (e) 24 h, (f) 48 h.

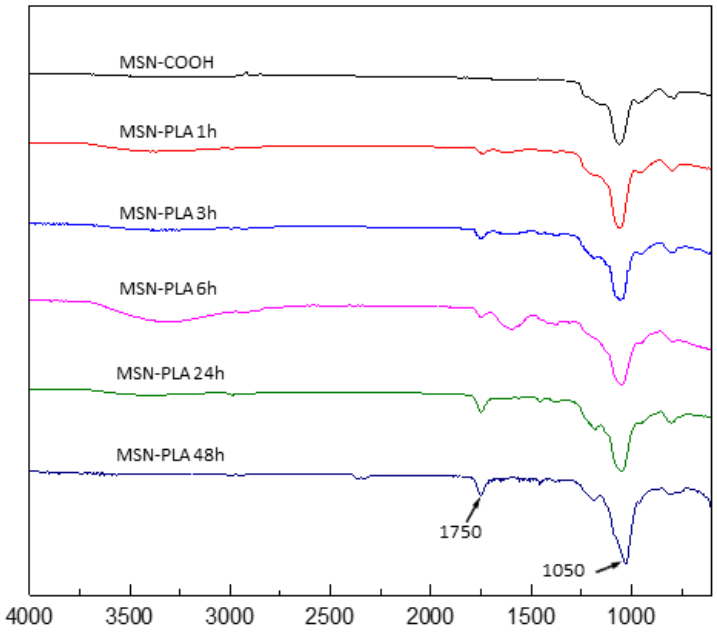

Figure 9. FTIR spectra of graft from MSN-COOHs and 1 h/3 h/6 h/24 h/48 h groups.

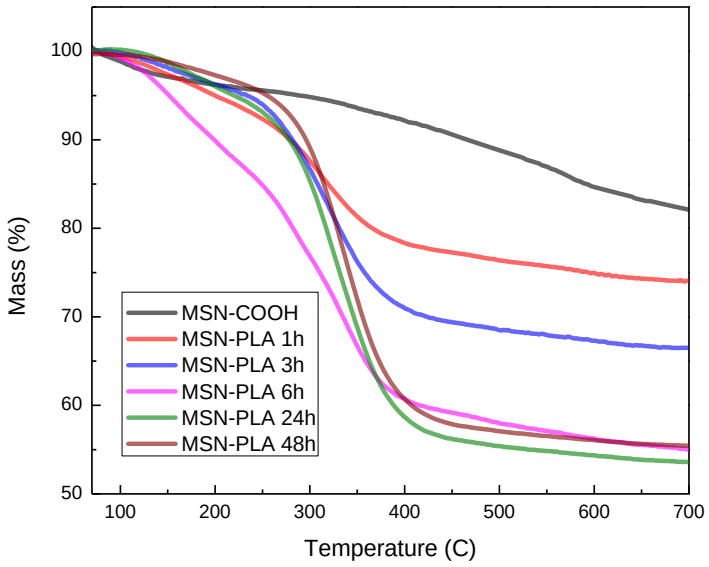

Figure 10. TGA analysis of MSNs and 1 h/3 h/6 h/24 h/48 h/10 d groups.

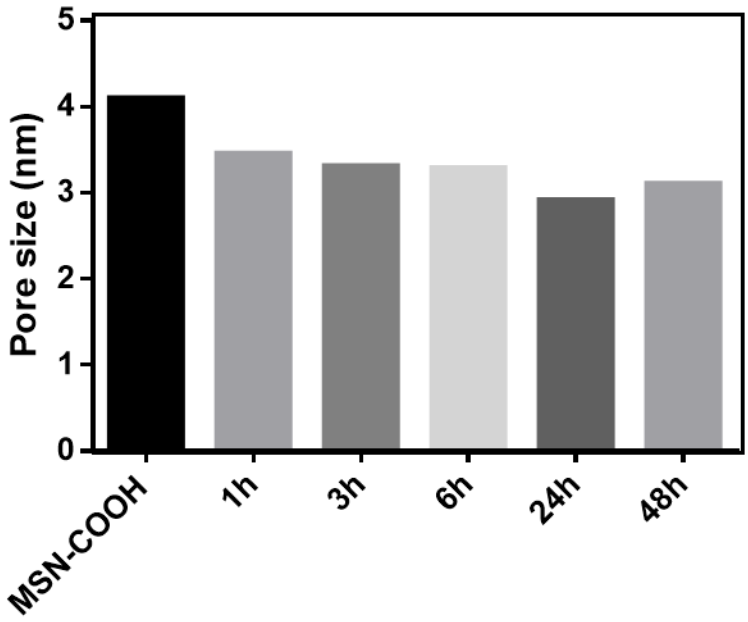

Figure 11. BET analysis of MSN-COOH, MSN-PLA 1 h/3 h/6 h/24 h/48 h groups. The time stands for various reaction time of lactide addition polymerization.

Hence, we moved on to another functionalization method for MSNs. The graft from approach is a bottom-up synthesis route as it involves the *in situ* polymerization of monomers on the nanoparticle surface, then propagation to lengthen each grafted chain[49]. The graft from approach sees much more success due to its higher reactivity. We have purchased a different set

of MSNs with surface -COOH groups for initiation of addition polymerization of lactides. Although it has less precise grafting length of polymer brushes, both the grafting density and ease of reaction is improved. We verified the PLA functionalization through FTIR spectrum, where a strong C=O peak can be observed, as well as an increasing amount of combusted PLA in different MSN-PLA groups as the polymerization time increased. Additionally, BET analysis showed that the average pore size of MSNs decreased as reaction time increased, suggesting that the grafted PLA brushes increased in length the longer it was allowed to react. The smaller pore sizes would lessen the drug leakage after loading into the pores of the nanoparticle, and contribute towards sustained release over a longer period of time.

4.1.2 Loading kinetics of nanocarriers

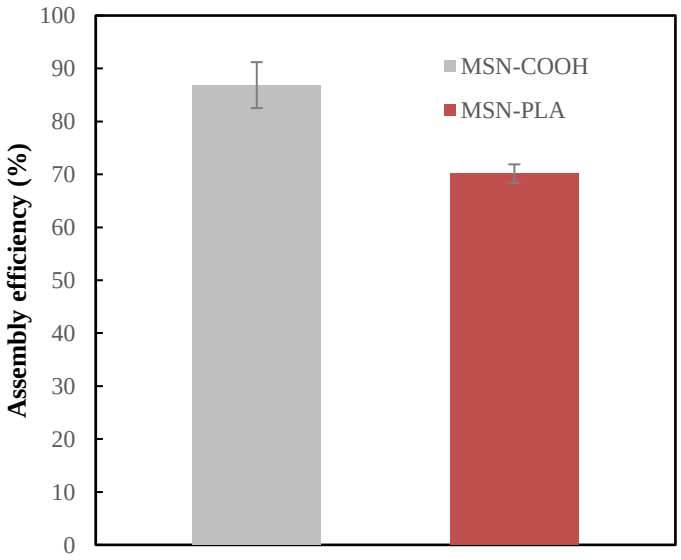

Figure 12. Self-assembly efficiency of Dox into MSN and MSN-PLAs in DI water.

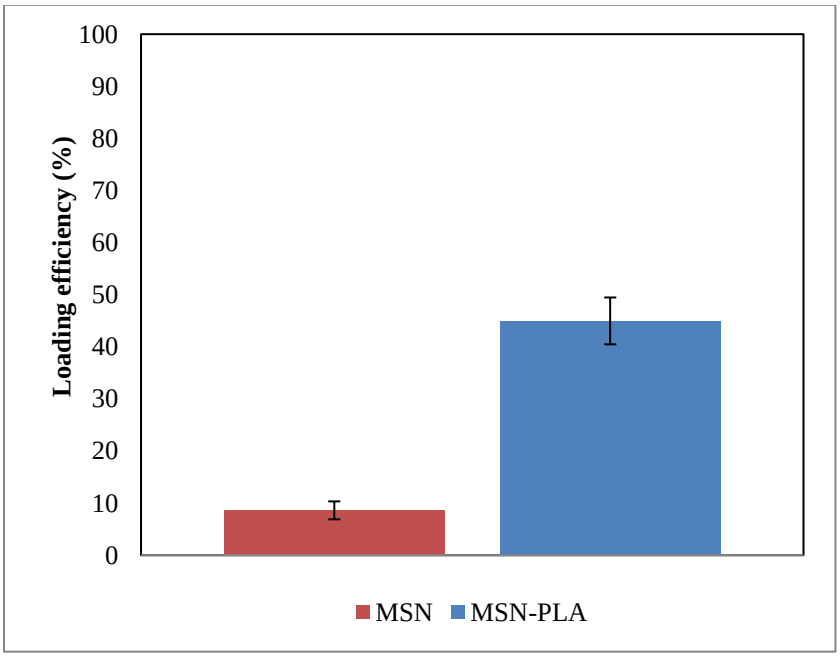

Figure 13. Loading capacity of MSN-COOHs and MSN-PLAs with HFIP dissolved Dox at 50 mg/mL.

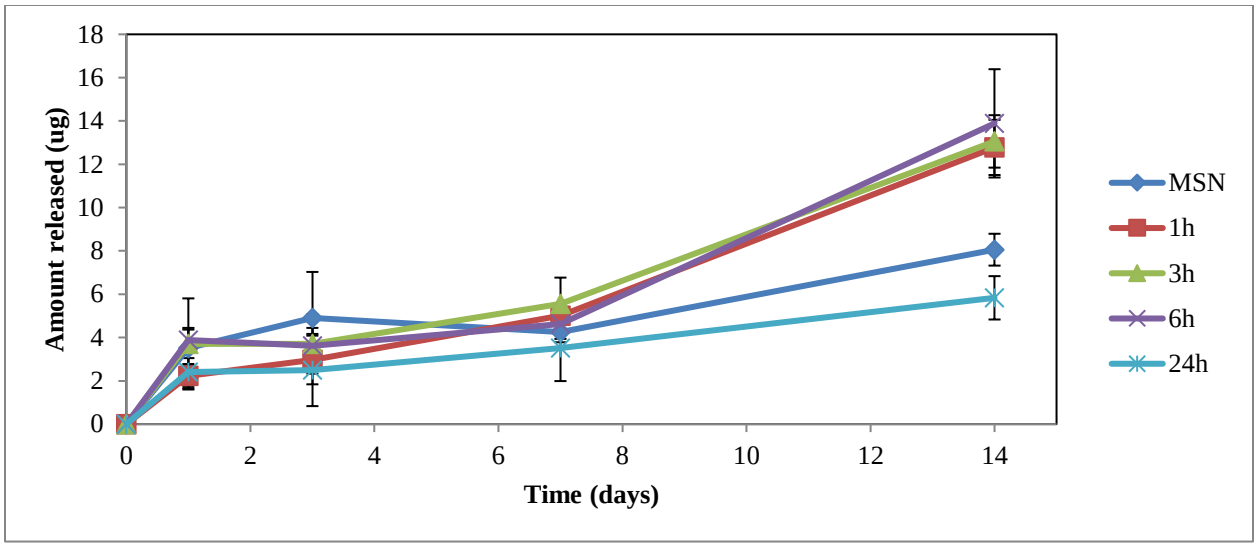

Figure 14. Short term release profile of MSNs and MSN-PLAs with various reaction lengths.

After establishing the nanocarriers for drug encapsulation, we moved on to the experimentation of loading mechanisms. We have attempted the loading of 5-fu into the nanoparticle pores, but the lack of electrostatic interactions caused severe drug leakage over 1 day. Thus, we have chosen another model drug for the study. Doxorubicin possesses amine groups on one end, which grants it good polarity and ionic interactions with the abundant hydroxyl and carboxyl groups on both the nanoparticle and polymer surface. Hence the drug retention and loading can utilize this mechanism to achieve passive loading. Self-assembly of 10 mg/mL Dox in water into MSNs was experimented to assess the electrostatic interactions between Dox and carboxyl groups on MSN and PLA surface. It showed very good affinity as most of the free drug molecules converged within the nanoparticle pores. This indicates the loading mechanism is based on electrostatic interactions between the positive end of amine group and the negative charge of the MSN and PLA brushes. Notably, the PLA group was able to load less Dox owing to the decrease in pore lumen size. We then loaded the MSN and MSN-PLAs with 50 mg/mL Dox-HFIP to extend the polymer brushes and maximize the drug loading capacity. Unsurprisingly, MSNs without polymer brushes were unable to retain much Dox within their pores while the PLA brushes were successful at preventing Dox from being washed out from the MSN pores, achieving around 50% loading efficiency despite the high concentration of Dox. Next, we performed drug release profile of nanoparticles to assess the drug diffusion speed between all groups, and we can see that at 24 h polymerization duration, the drug release becomes slower than bare MSNs yet their drug loading capacity is around 5 times of bare MSNs.

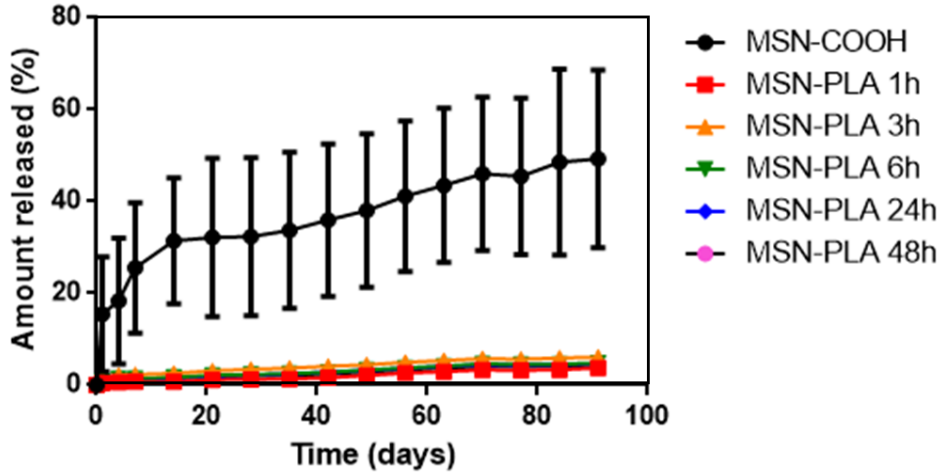

Figure 15. Dox release profile of MSN-COOH, MSN-PLA 1 h/3 h/6 h/24 h/48 h.

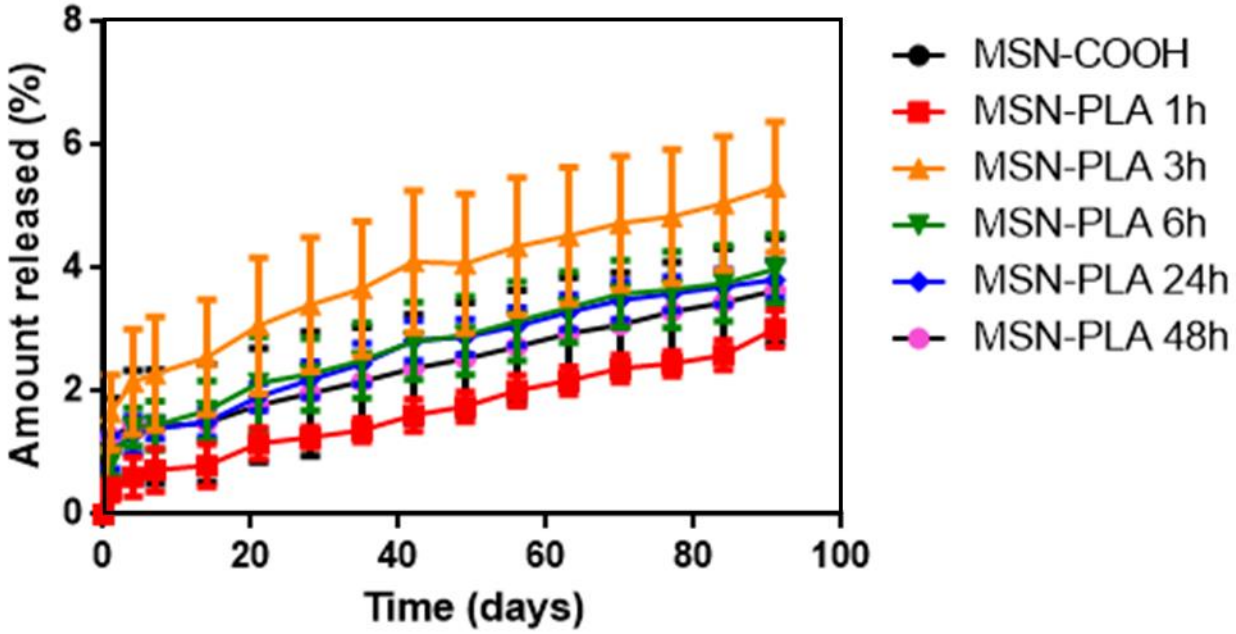

Figure 16. Dox release profile of MSN-PLA 1 h/3 h/6 h/24 h/48 h.

Next, we performed the long-term drug release assessment of Dox from various MSN-PLA groups. Compared with MSNs with PLA brushes grafted on their surfaces, the bare MSN-COOHs displayed significant leakage when submerged in water over 3 months, meanwhile owing to the lock-and-key mechanism of PLA brushes, the amount of Dox released to the

surroundings are much lower. This indicates the release mechanism of Dox is based on the small molecule diffusion and the slow degradation of PLA, and shows that our PLA-grafted MSNs are successful at gatekeeping drug molecules from passive leakage into the surrounding aqueous environments.

4.1.3 Cytotoxicity assessment of nanocarriers

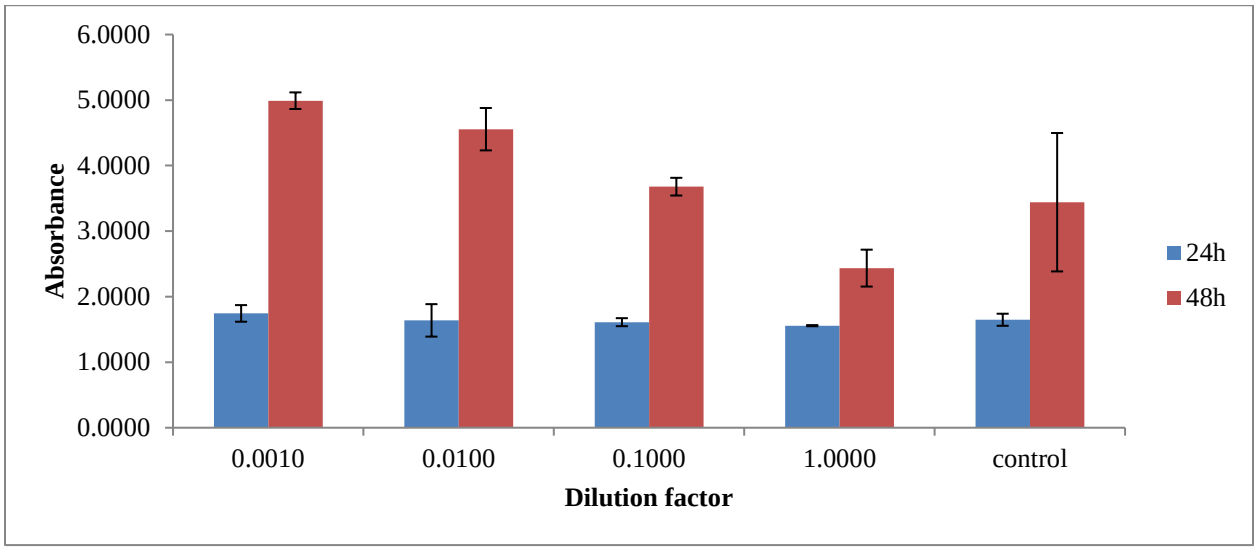

Figure 17. CCK-8 assay of MSN-PLA-Dox.

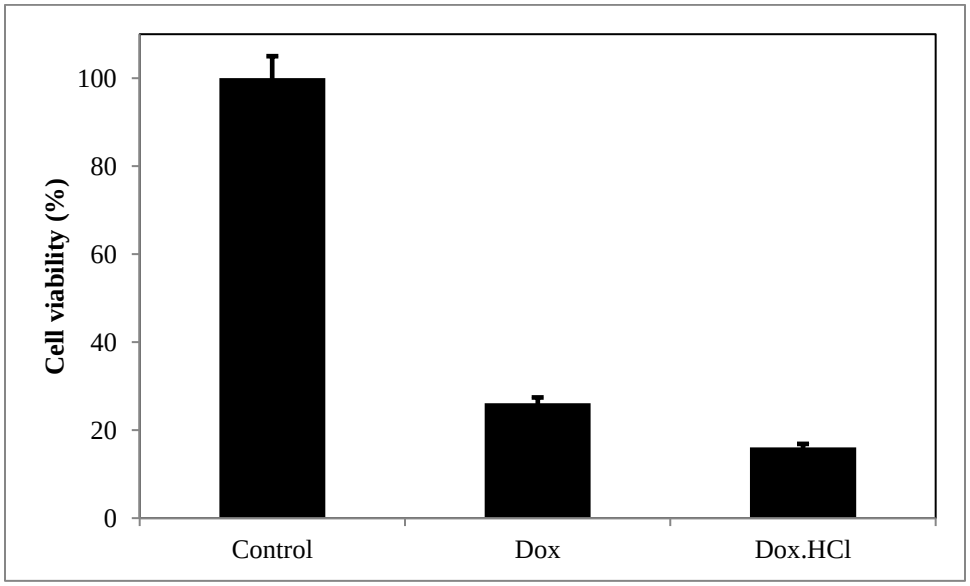

Figure 18. Cytotoxicity test of organic Dox and aqueous Dox.HCl. Cell viability was quantified by number using fluorescence of living cells by calcein AM staining.

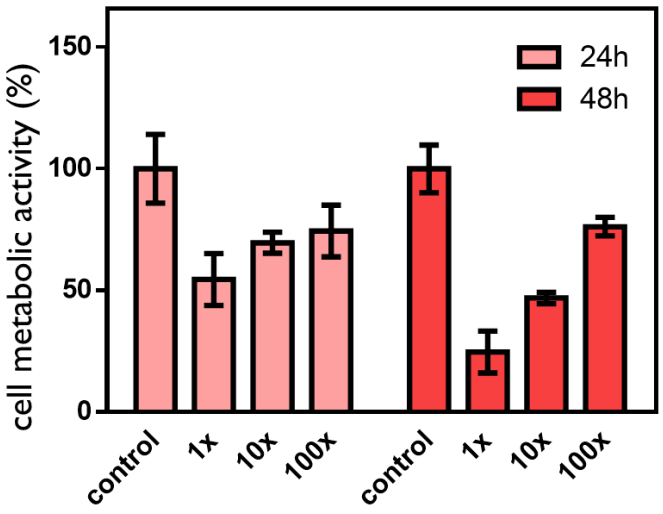

Figure 19. CCK-8 assay of MSN-PLA-Dox.HCl with 1x/10x/100x dilution of Dox-infused culture medium.

To reflect the anti-scarring efficacy of the nanocarriers at the pathological wound bed of a healing wound, cell culture experiments were performed with 3T3 human fibroblasts. To simulate the effect of loading MSNs in electrospun fibers, indirect contact cytotoxicity test was performed according to the international standards for biomedical devices. Briefly, MSNs were incubated using culture medium for 24 h before introduction to pre-seeded 3T3 fibroblasts in culture well plates for 24 and 48 h. While results were not significant at 24 h, MSN-PLA-dox was able to reduce proliferation of fibroblasts after incubation for 48 h. We suspect that this may be caused by low activity of Dox at lower concentrations. We then assessed the cytotoxicity of two types of Dox: the organic form Dox and aqueous Dox.HCl. It was observed that Dox.HCl was more effective at inhibiting fibroblast growth with the least cell spreading area, as well as rapid apoptosis as cell fragments could be observed within the culture medium after 24 h. With this we switched to Dox.HCl and repeated the same experiments using MSN-PLA-Dox.HCl, and yielded good results with significant fibroblast inhibition even at much diluted concentrations of dox-medium. Hence, Dox.HCl was used for all further cytotoxicity studies.

4.1.4 Physical characterization of electrospun skin scaffolds

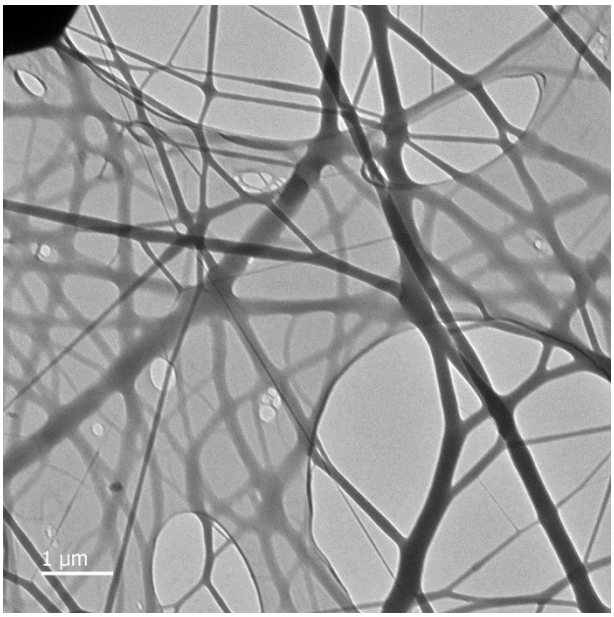

Figure 20. TEM image of HA/PLA emulsion fibers.

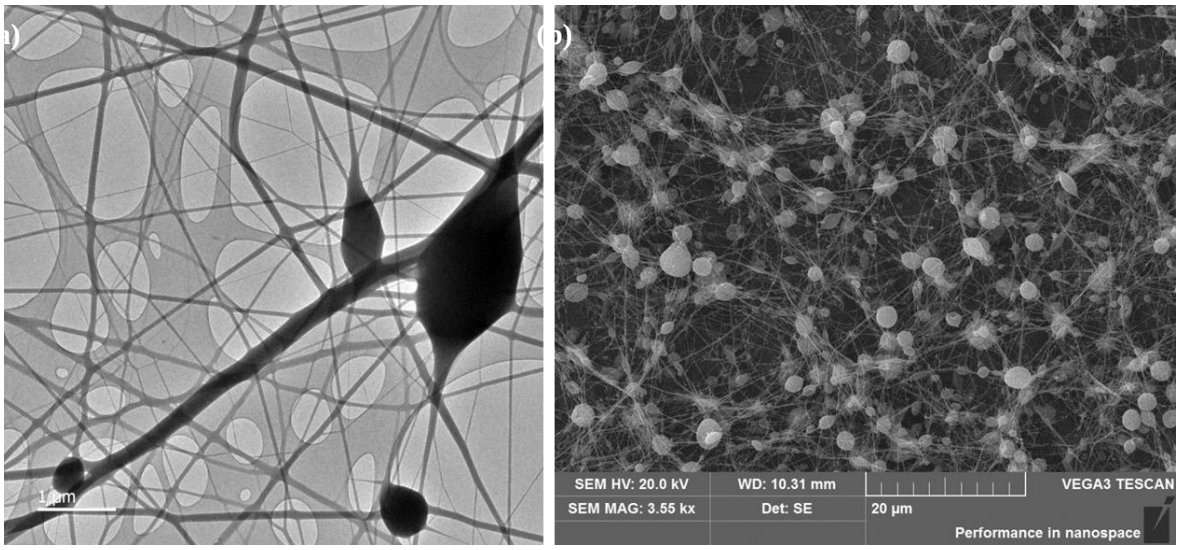

Figure 21. (a) TEM and (b) SEM image of HA/PLA co-axial fibers

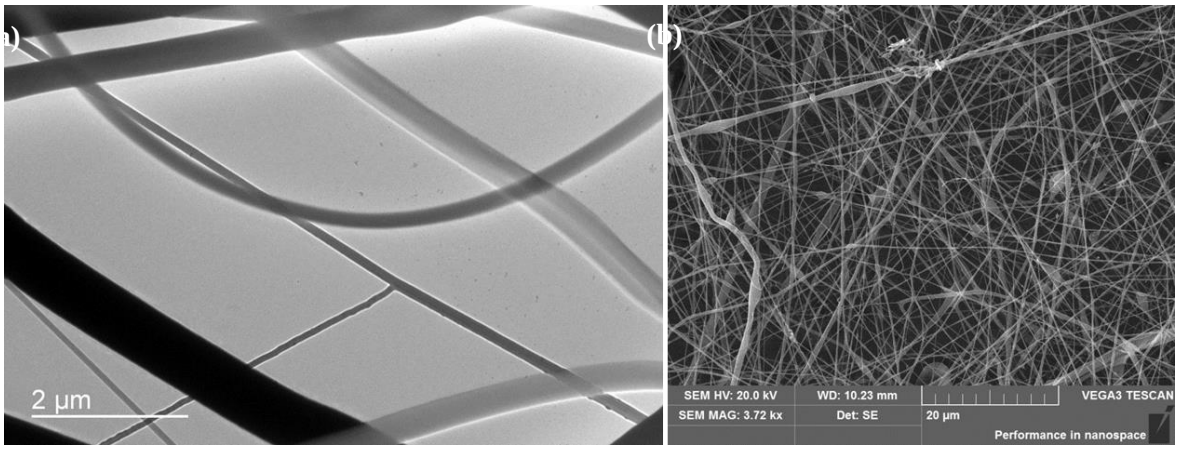

Figure 22. (a) TEM and (b) SEM image of gelatin/PLA co-axial fibers

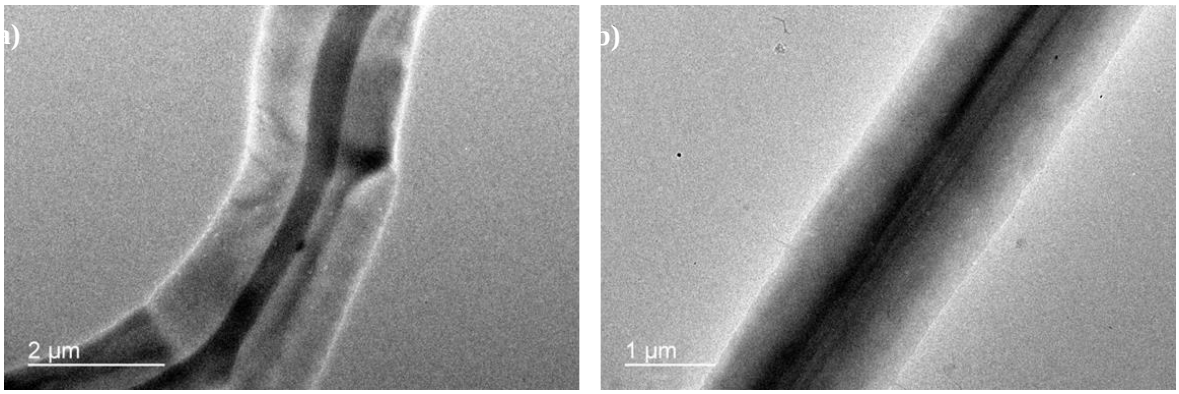

Figure 23. TEM image of (a) pre-dried and (b) dried PVA/PCL co-axial fibers.

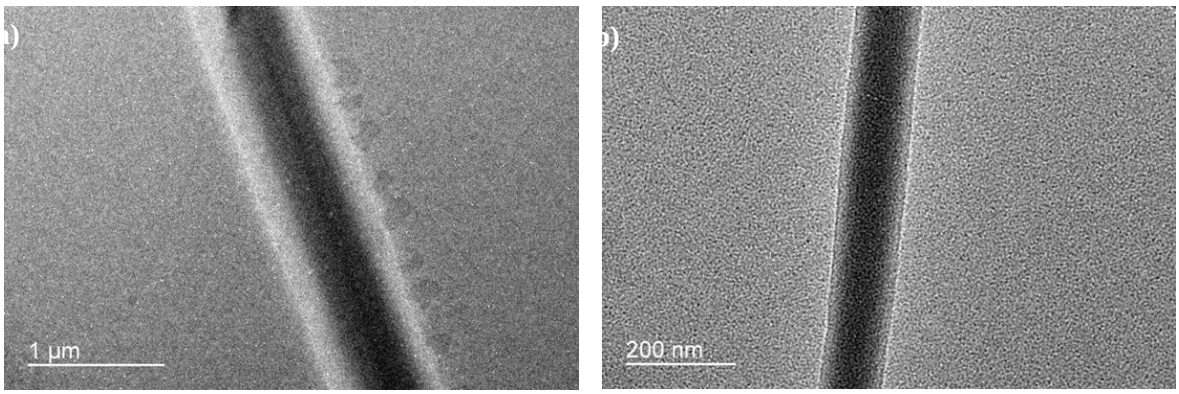

Figure 24. TEM image of (a) pre-dried and (b) dried ethanol/PLA co-axial blend fibers.

After establishing the anti-scarring potential of Dox encapsulated carriers, they require a bulk structure to achieve localized release and further extend the drug diffusion distance for sustained release. Core-sheath and emulsion electrospinning was chosen owing to its capacity to stagger the release of loaded content compared with blended fibers. HA was originally chosen as the aqueous core due to its clinical significance in wound healing. However, while HA/PLA emulsion fibers were successfully fabricated, no core-shell structure can be observed in the fibers. We also attempted co-axial spinning of HA with PLA, and could only form droplet structures due to the poor spinnability. We suspect that the high viscosity of HA despite its low concentration in solution causes this. We then experimented with gelatin electrospinning as it itself is a good spinnable polymer even when dissolved in aqueous solvents. Gelatin PLA co-axial fibers were successfully synthesized with much less droplet structures in the fiber network. However, from the TEM image we observed that gelatin and PLA were separately deposited onto the receiver, showing that gelatin are not enveloped in PLA during spinning. Hence, we attempted to perform co-axial electrospinning with a good spinnability core and poor spinnability shell. With this, PVA/PCL co-axial fibers were synthesized. As PVA is dissolved using water, we could add an ionic TEM dye ammonium molybate to better visualize the inner structure of the fibers. From the microscopic images, we could clearly observe distinguished core-shell structures using this approach. We also attempted electrospinning using blank core solutions as we tried to replicate studies that use DI water as core solvents for their co-axial electrospinning [50]. Nevertheless, we could not replicate the results using DI water, but ethanol with much lower surface tension can be mixed with the PLA solution to form a pseudo-blend core-shell fiber which has core-shell structures that disappeared after evaporation of ethanol. Thus, we move on to adding MSNs to the aqueous core of the spinning solutions of PVA/PCL and ethanol/PLA fibers.

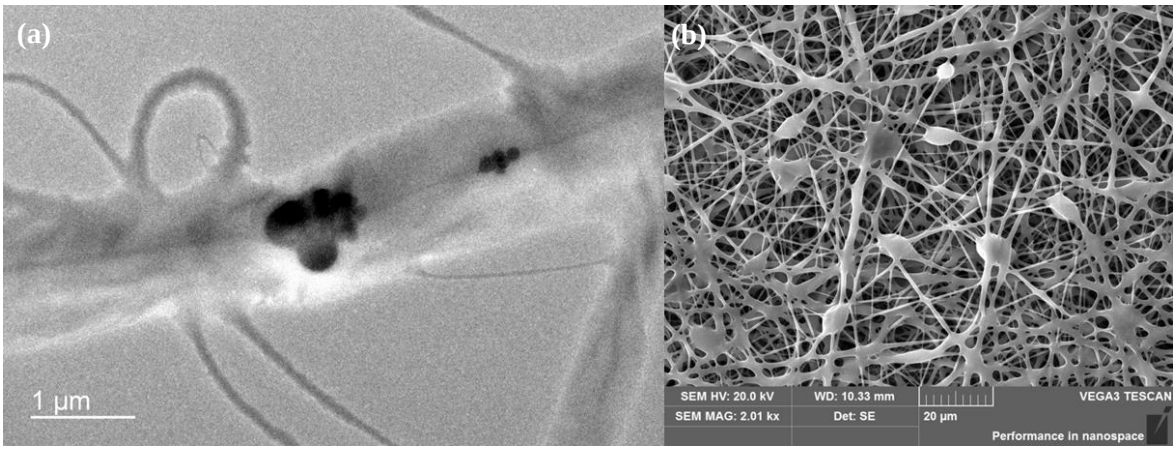

Figure 25. (a) TEM and (b) SEM image of PVA-MSN/PCL co-axial fibers.

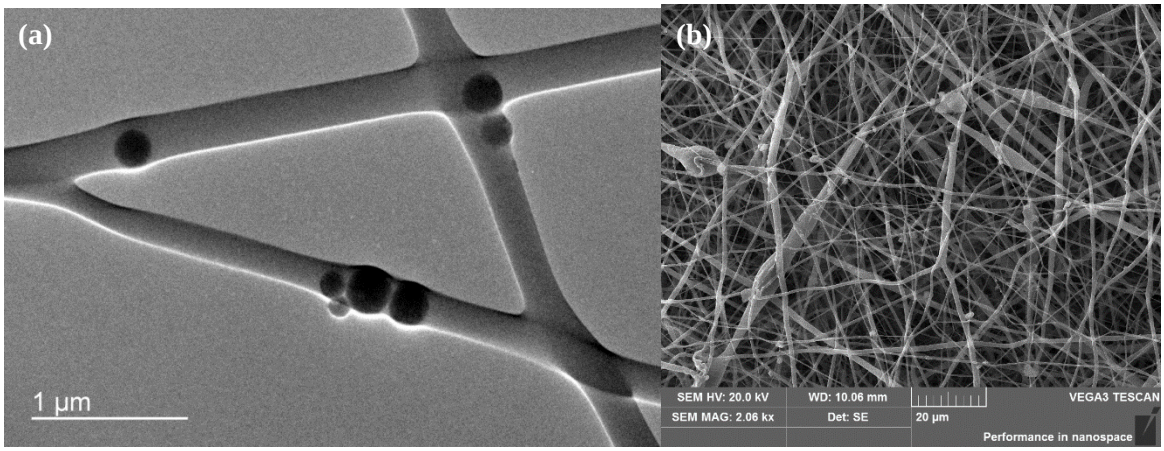

Figure 26. (a) TEM and (b) SEM image of ethanol-MSN/PLA co-axial blend fibers.

With no surprise, after adding MSNs to the viscous PVA solution, its spinnability is greatly hindered, showing frequent clogging and inconsistent fiber formation. This greatly limits the fiber loading capability of MSNs. On the other hand, ethanol MSN PLA fibers perform relatively similar to its unloaded counterpart even at high MSN concentrations, and are able to encapsulate MSNs within the fiber lumen with consistent fiber structures after drying. We would need to experiment with higher concentrations of PLA to increase fiber diameter, but overall the morphology and loading capability is the most successful so far possibly due to the absence of any viscous matter in the aqueous core.

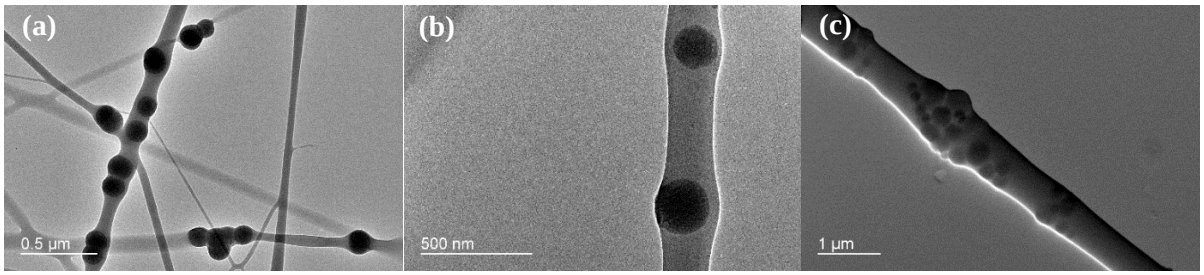

Figure 27. TEM image of (a) 10%, (b) 20%, and (c) 30% PLA fibers with 50 mg/mL MSNs.

We experimented with different concentrations of PLLA in solvent to tune the diameter of fibers to contain the MSNs within. After observing the fibers at different concentrations, we have selected 30% PLA as the concentration as it creates the fibers with the highest diameter to envelop the MSNs with, which greatly increases the diffusion distance between the drug molecule and the immersed fluids.

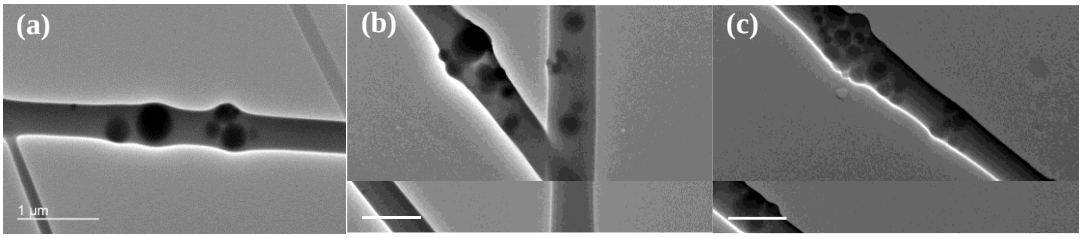

Figure 28. TEM image of 10 mg/mL, 20 mg/mL and 50 mg/mL MSNs 30% PLA fiber.

Next, we tuned the concentration of MSNs within the electrospun fiber lumen. The amount of MSNs added to the electrospinning solution greatly affected the kinetics of the fiber formation, and is reflected in the fiber morphology of the resultant scaffold. The diameter of fibers increased with the amount of nanoparticle content added, as well as the exposure of particle surfaces to the edge of the fibers. These varied morphologies directly impact the mechanical properties and drug retention capabilities of the electrospun scaffold.

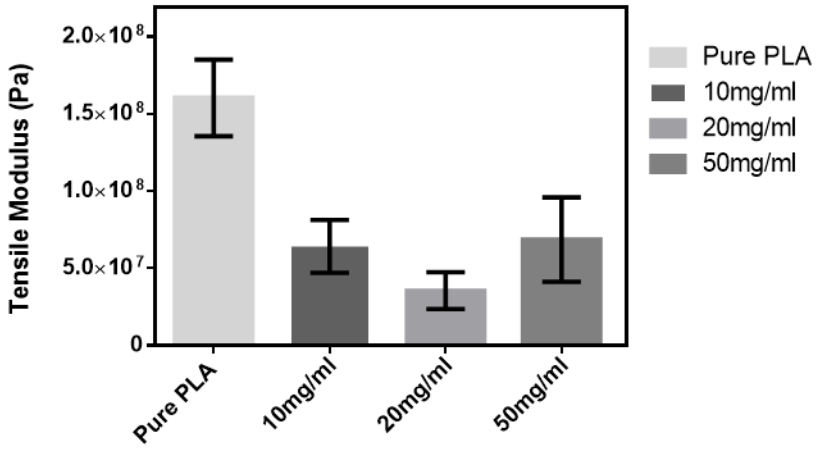

Figure 29. Tensile modulus of varied MSN concentrations in 30% PLA fibers.

The addition of MSNs into the lumen of the electrospun fibers greatly varied its mechanical properties. 20 mg/mL displayed the lowest tensile strength as the high inclusion of MSNs in the fiber greatly reduced its elasticity. The effect is lowered in 10 mg/mL groups as less of the PLA content was replaced by inelastic and brittle MSNs. For 50 mg/mL, however, the high concentration of MSNs in the electrospinning solution reduced its spinnability, thus forming thicker fibers than the other 2 groups. This have led to the formation of stronger fibers with the highest MSN content out of the 3.

4.1.5 Loading and release kinetics of electrospun skin scaffolds

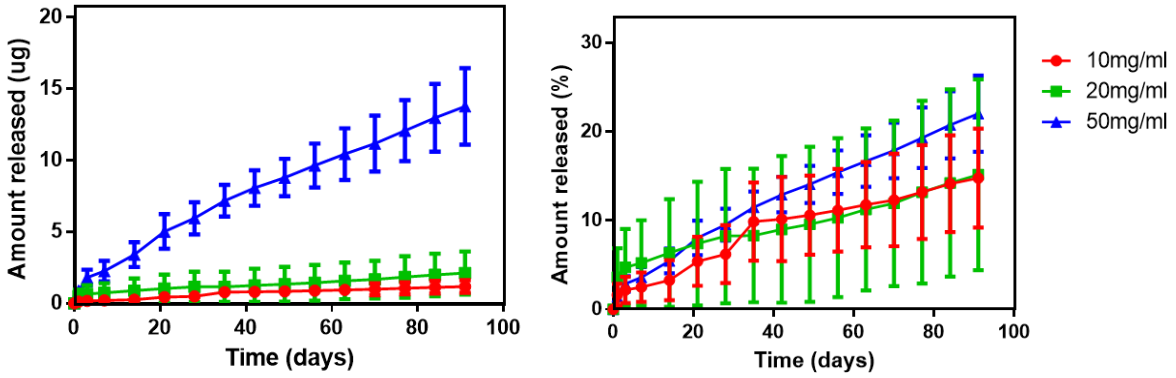

Figure 30. Dox release profile of 10 mg/mL, 20 mg/mL, 50 mg/mL MSN-PLA-Dox fibers.

The MSN-PLA-Dox loaded fibers were then characterized with long-term drug release assessment by immersion in PBS over 90 days with replacement of fluids at fixed time intervals. The morphological changes are greatly reflected in the release profile of encapsulated Dox. 50 mg/mL, as the group with the highest MSN-PLA-Dox concentration, steadily released more Dox over 90 days compared to the other 2 groups. However, the release kinetics among the 3 groups are relatively similar, with 50 mg/mL releasing slightly faster owing to the surface exposure of MSNs. This possibly create problems with excessive inhibition of fibroblasts which affects the healing efficacy of open wounds, and thus dosage control is extremely important to ensure the complete healing of cutaneous wounds.

4.1.6 *In vitro* cytotoxicity assessment of electrospun skin scaffolds

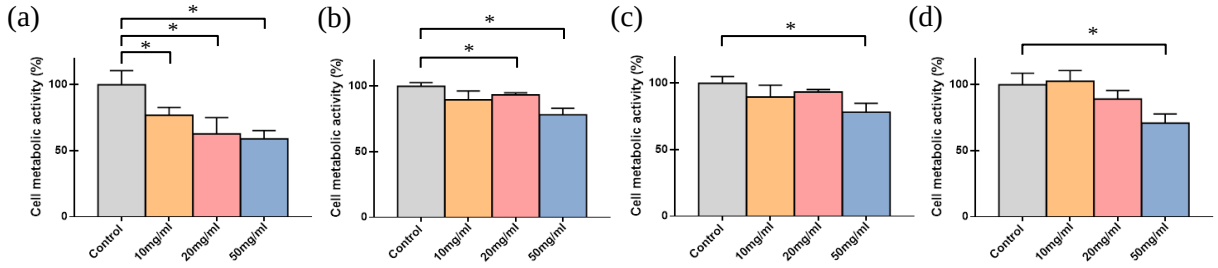

Figure 31. CCK-8 assay of10 mg/mL, 20 mg/mL, 50 mg/mL MSN-PLA-Dox fibers over (a) 0, (b) 30, (c) 60, (d) 90 days. (n = 3 for each sample, *p < 0.05).

After verification of the long-term drug release profile of the fibers, we assessed whether the released Dox exhibit enough dosage to inhibit fibroblast activity using cell proliferation assay. The CCK-8 assay results demonstrated that 50 mg/mL groups were consistently able to significantly inhibit cell activity while the 10 mg/mL and 20 mg/mL group's dosage may be too low to make significant impact on cell proliferation after the initial burst release.

While inhibition of fibroblast activity is important, the adhesion of fibroblasts on the wound dressing is still important to achieving wound closure and completing the wound healing cycle. As such the Dox concentration cannot be overly cytotoxic where it directly renders the cells incapable of performing reparative functions. Hence, we performed the cytoskeletal staining with phalloidin and DAPI for verification of scaffold biocompatibility.

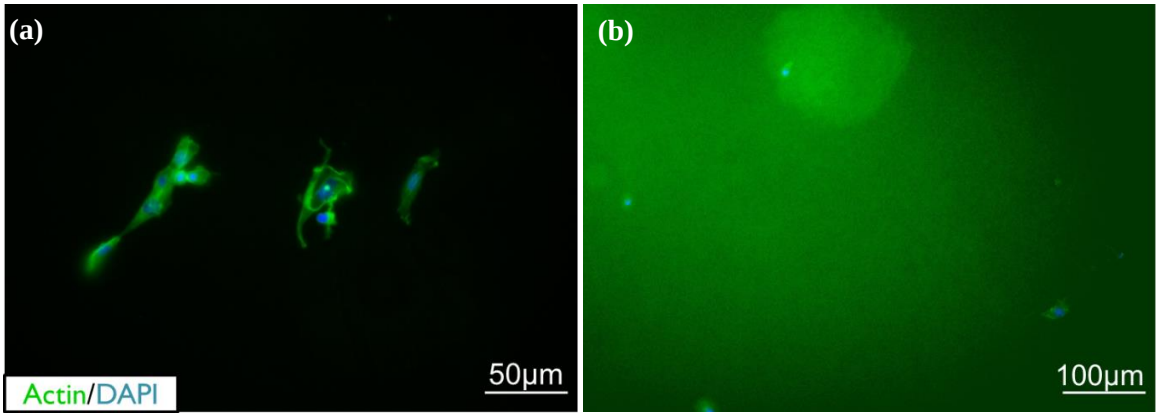

Figure 32. Actin-DAPI staining of 3T3 adhesion on (a) pure PLA membrane and (b) PLA/MSN-PLA-Dox membranes with phalloidin 488.

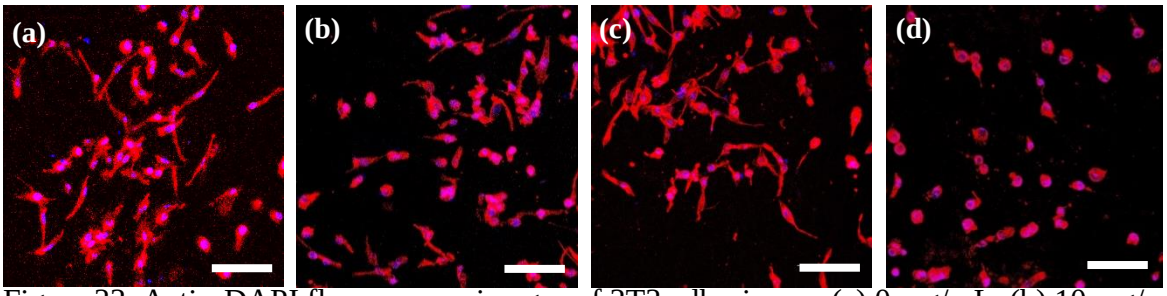

Figure 33. Actin-DAPI fluorescence images of 3T3 adhesion on (a) 0 mg/mL, (b) 10 mg/mL, (c) 20 mg/mL, 50 mg/mL MSN-PLA-Dox fibers on day 0. (scale bar = 200 µm)

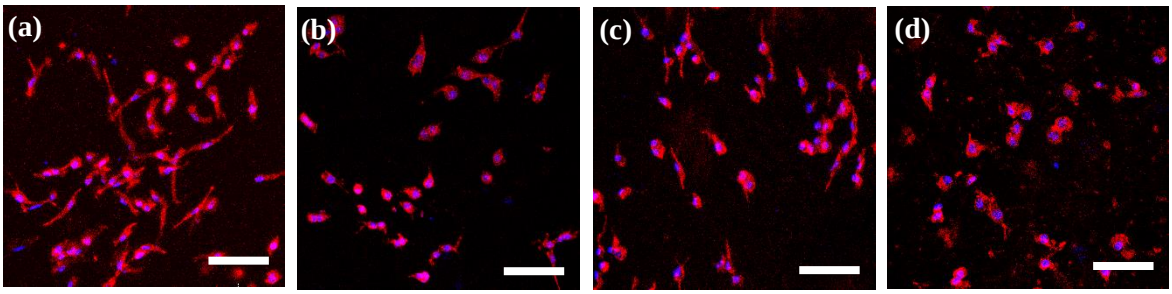

Figure 34. Actin-DAPI fluorescence images of 3T3 adhesion on 0 mg/mL, 10 mg/mL, 20 mg/mL, 50 mg/mL MSN-PLA-Dox fibers on day 90. (scale bar = 200 µm)

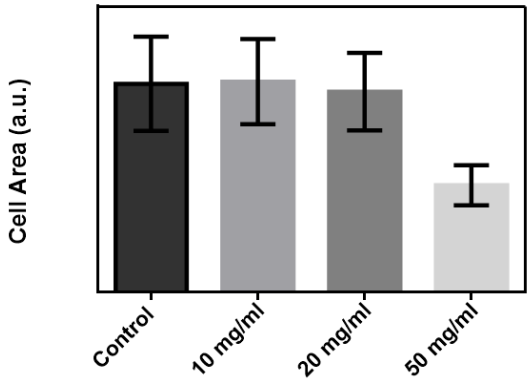

Figure 35. Quantification of average area per cell of 3T3 fibroblasts adhered on electrospun scaffolds.

Originally, phalloidin 488 was used for actin staining of fibroblasts. However, owing to the fluorescence spectrum overlap between Dox and phalloidin 488, the background noise of cytoskeletal images was very strong. Thus we switched to a red staining agent phalloidin 594, which yielded far better results. On day 0, fibroblasts adhered on 10 mg/mL, 20 mg/mL and 50 mg/mL exhibited clearly smaller spreading area compared with the control group with no MSN-Dox. It can also be observed that the cell density on 50 mg/mL is significantly lower than the

other groups, in accordance with the cell proliferation data. On day 90, the same reduction in spreading area could be observed, showing that the continuously released Dox was able to inhibit fibroblast proliferation without directly hindering their cellular functions for a long time. With these promising results, we moved onto animal models of hypertrophic scarring with 20 mg/mL and 50 mg/mL groups to demonstrate the clinical relevancy of our long-term drug release fibrous scaffold under an *in vivo* setting.

4.1.7 *In vivo* anti-scarring efficacy assessment of electrospun skin scaffolds

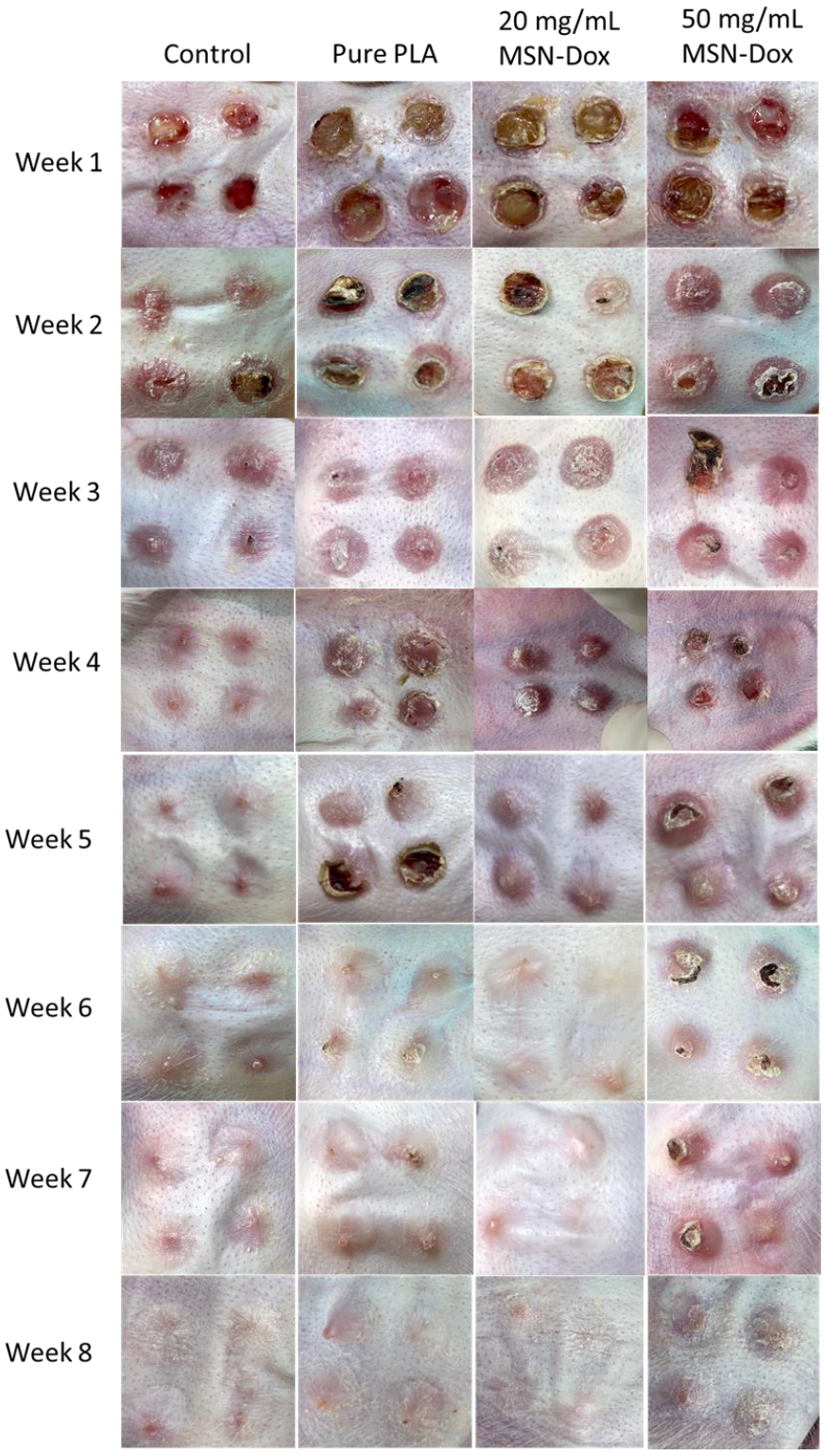

Figure 36. Photographs of healing wounds and scar tissues of rabbit ear hypertrophic scar model treated with no treatment, pure PLA, 20 mg/mL and 50 mg/mL MSN skin scaffolds.

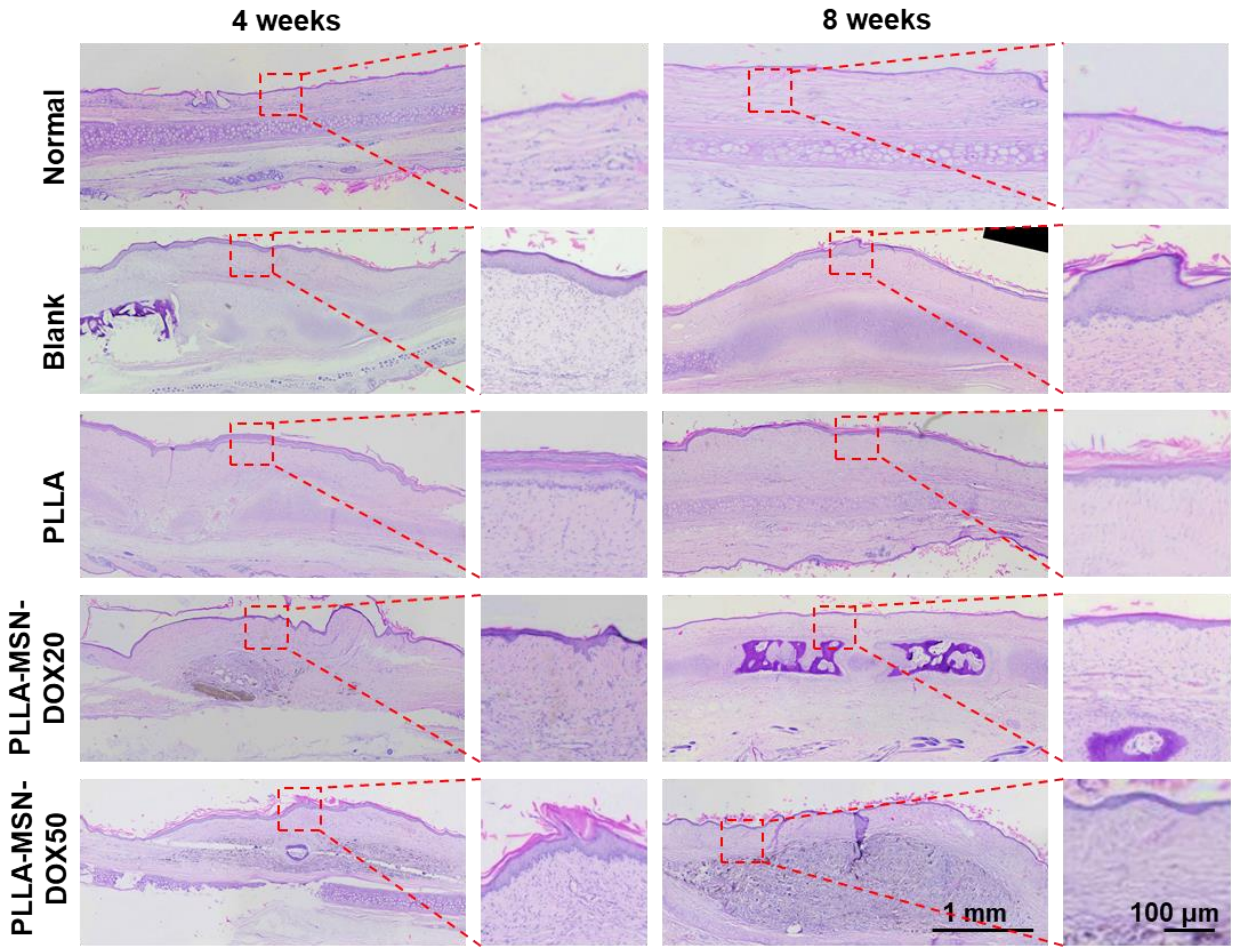

Figure 37. Hematoxylin and eosin stained microscope images of different treatment groups. (Nuclei = purple, ECM & cytoplasm = pink)

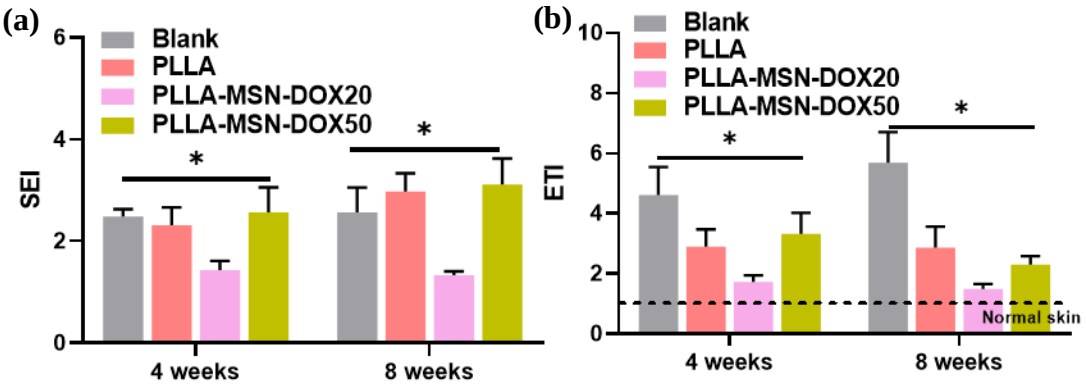

Figure 38. Quantification of (a) scar elevation index (SEI) and (b) epidermal thickness index (ETI) of rabbit ear scar tissues.

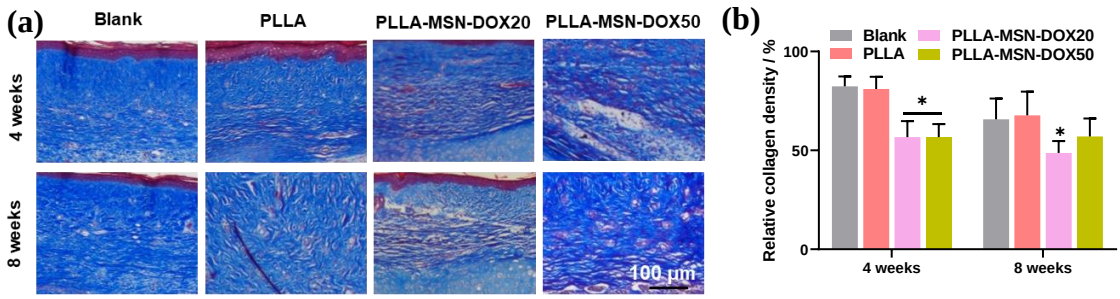

Figure 39. Masson's Trichrome stained (a) microscopic image and (b) collagen quantification of various treatment groups.

Based on the effectiveness of fibroblast inhibition in the *in vitro* study, we selected 20 mg/mL and 50 mg/mL MSN-PLA-Dox groups as the experimental groups for small animal study as they demonstrate the stronger inhibitory effects owing to the higher dosage of Dox encapsulated, while 10 mg/mL may have too low of a drug dosage to produce significant inhibitory effects. Special acknowledgement and gratitude to collage Tianpeng Xu and Richard Dong for completing the small animal experiments. Throughout the entire animal study, wound enclosure is achieved by every group, with 50 mg/mL group displaying delayed healing. Meanwhile, 20 mg/mL displayed to flattest healed tissues out of all the groups, suggesting its increased efficacy at scar inhibition. In H&E stained tissues, 20 mg/mL groups also displayed the lowest SEI and ETI out of all groups, which demonstrates that the sustained release of Dox was helpful to inhibit formation of granular tissues. In Masson's Trichrome stained scar tissues, both 20 mg/mL and 50 mg/mL groups displayed significantly lowered collagen deposition. However, the 50 mg/mL as observed earlier induced hyperplasia in the healing tissues, causing increased thickness and proliferation of fibroblasts. This suggests that the sustained release of doxorubicin is able to inhibit scar formation, but only at certain dosages. Notably, the 20 mg/mL displayed superior anti-scarring effects in rabbit ear hypertrophic scar models, with healed epidermal thicknesses most similar to healthy rabbit skin. These results showed that our long-term drug release scaffold is able to achieve effective anti-scarring under clinical settings.

4.2 Artificial periosteum with osteogenic-angiogenic coupling for treatment of fractures

4.2.1 Chemical and physical characterization of nanocarrier

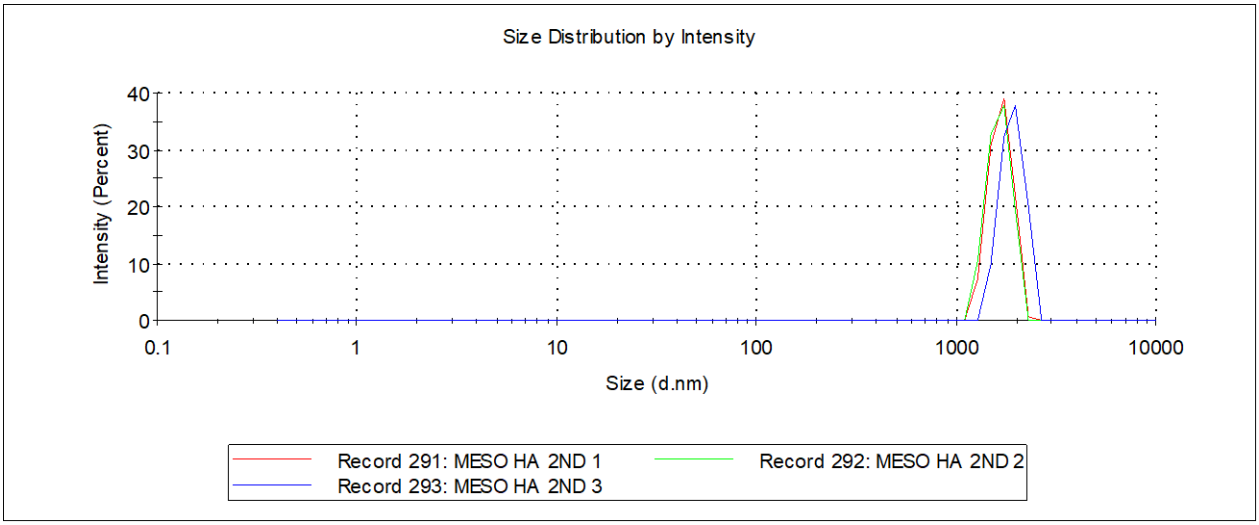

Figure 40. DLS distribution of mesoporous hydroxyapatite (meso HA) nanoparticles.

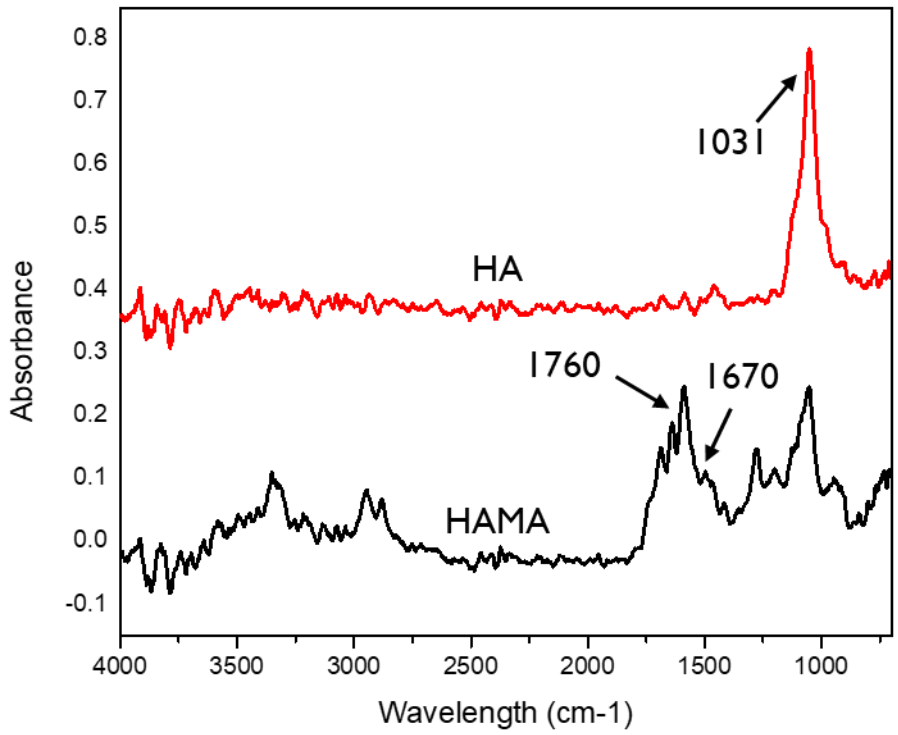

Figure 41. FTIR spectrum of pure meso HA and HAMA nanoparticles.

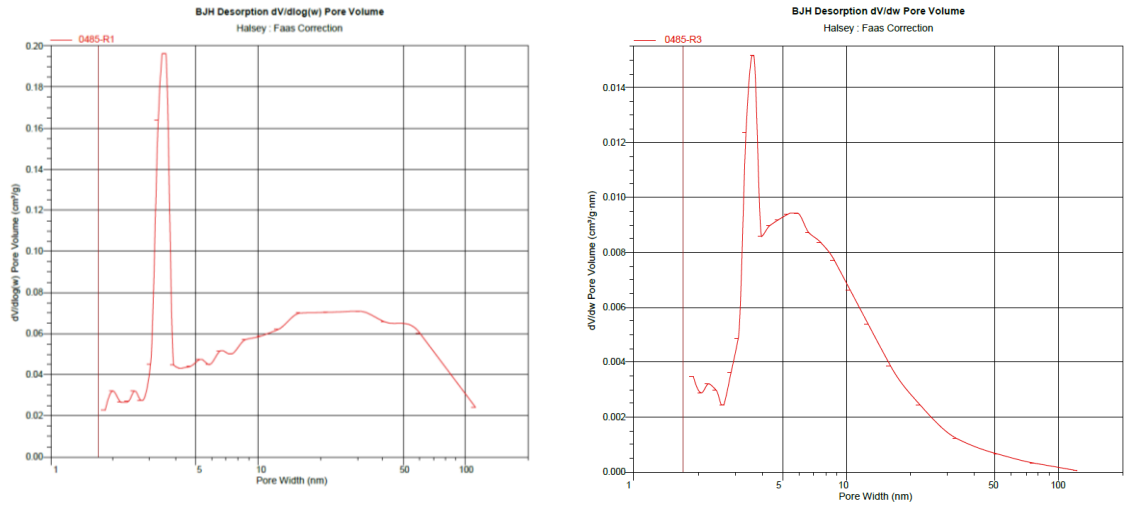

Figure 42. BET analysis of pure meso HA and HAMA.

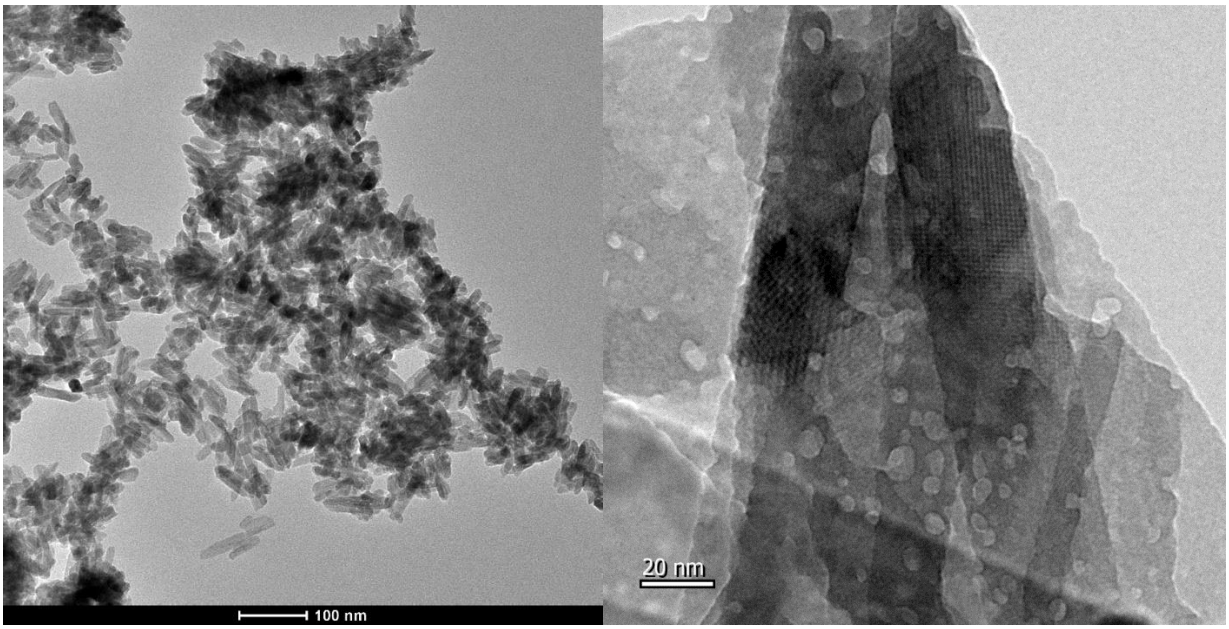

Figure 43. TEM images of meso HA nanoparticles.

To establish the nanocarrier for the artificial periosteum system, we first synthesized mesoporous hydroxyapatite nanoparticles (meso HA) using CTAB as template and mesitylene for enlargement of pores. After calcining, all the excess CTAB and unreacted substrates were removed from the porous nanoparticles, as evidenced by the pure HA spectrum of the resultant particles. BET analysis revealed that the average pore size of the resultant particles is around 3.59 nm, which is appropriate for drug encapsulation and sustained release. The formation of mesopores is further confirmed through TEM imaging, where pores of various sizes can be observed, as well as permeating mesopores in the crystal structure.

To further functionalize the meso HA with co-crosslinking properties, we attached HEMA chains on the surface using a simple click reaction. After thorough washing, FTIR spectrum confirms the functionalization through the C=O peak, while there is no visible difference in morphology or pore size in TEM and BET. Denoted as meso HAMAs, this establishes the physical and chemical composition of our nanocarrier in the artificial periosteum.

4.2.2 Physical characterization of electrospun periosteum scaffolds

Blending of meso HA in electrospinning is achieved through addition of 1% and 0.5% w/v meso HA in the electrospinning solutions. Under TEM imaging, it is observed that the addition of HA and L-arginine did not significantly affect the fiber formation. However, the added L-arginine contributes towards increased viscosity of the spinning solution, causing a general increase in fiber diameter and reduced stability of fiber ejection onto collector. This is circumvented through increasing spinning voltage (14-18 kV) in the experimental setup, which ensured that consistent fiber formation was deposited onto the collector over long periods of spinning.

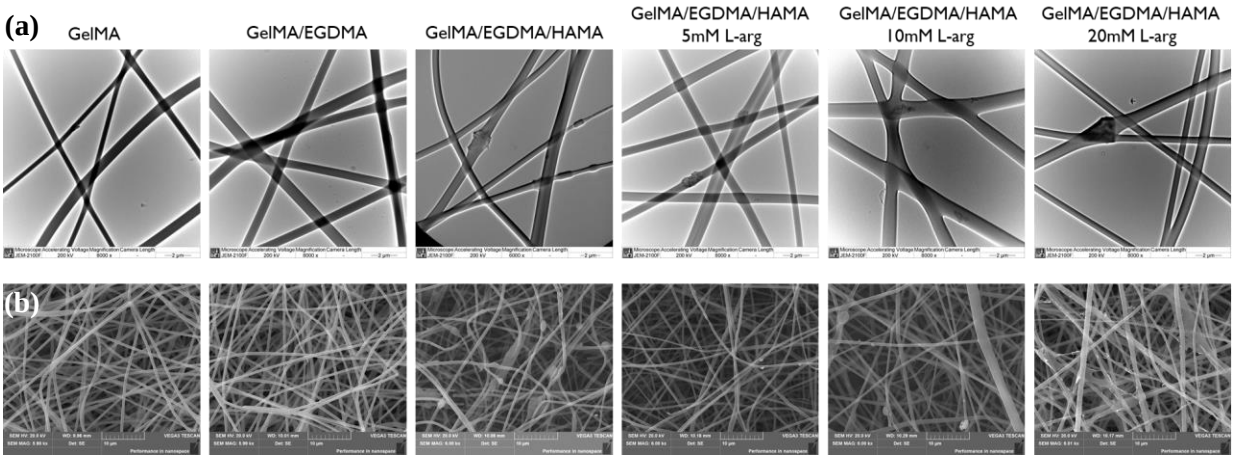

Figure 44. (a) TEM and (b) SEM images of electrospun GelMA, GelMA/EGDMA, GelMA/EGDMA/HAMA, GelMA/EGDMA/HAMA-5mM arg, GelMA/EGDMA/HAMA-10mM arg, GelMA/EGDMA/HAMA-20mM arg scaffolds.

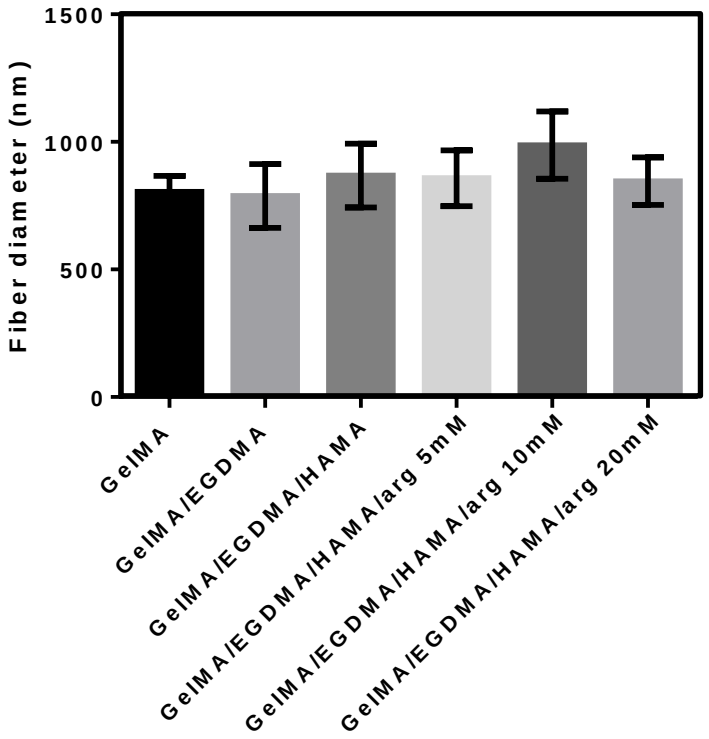

Figure 45. Quantification of fiber diameter of different periosteum groups.

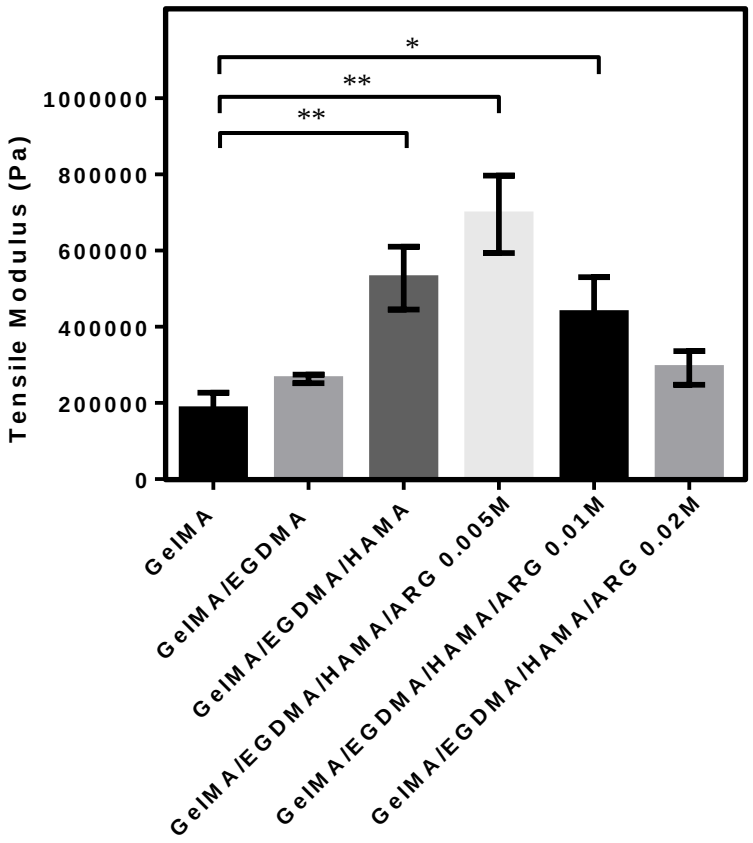

Figure 46. Tensile modulus of electrospun GelMA/EGDMA/HAMA-arg scaffolds. (n = 5 for each sample, *$p < 0.05$ and **$p < 0.01$).

Blending of meso HA in electrospinning is achieved through addition of 1% and 0.5% w/v meso HA in the electrospinning solutions. As aforementioned, the amount of solute in an electrospinning solution can greatly affect its bulk mechanical properties. The 1% meso HA addition, while increasing the mechanical properties of electrospun scaffolds, is much less effective than adding 0.5% w/v meso HA. Notably, the addition of EGDMA and HAMA were able to improve the mechanical property respectively, while the L-arginine effect on mechanical property is concentration-dependant. At 20 mM, the added viscosity interferes with stable spinning and caused a drop in mechanical property compared with no addition of L-arginine, while for 5 mM group the mechanical property is significantly enhanced.

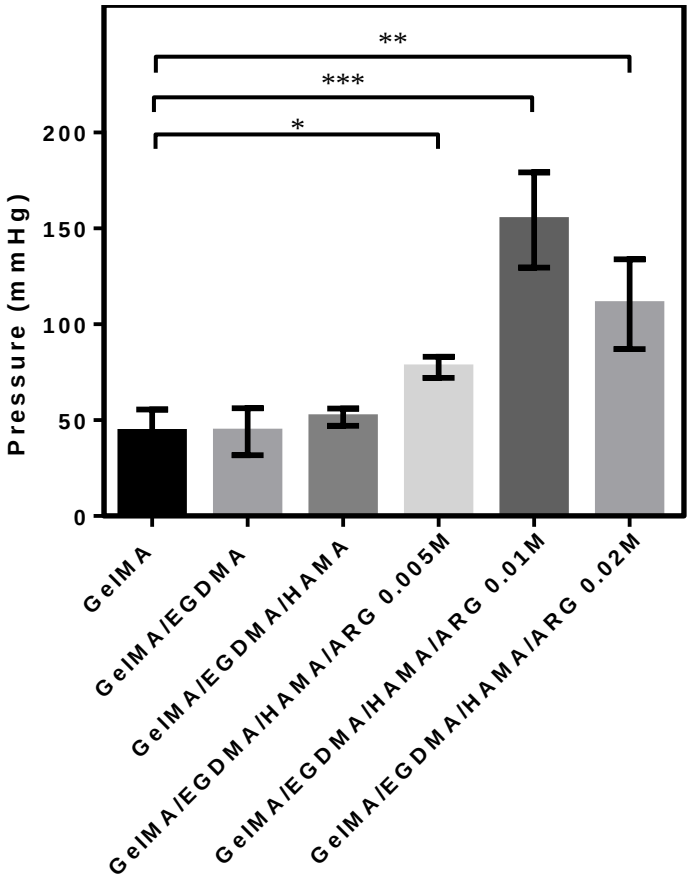

Figure 47. Quantification of burst pressure of electrospun GelMA/EGDMA/HAMA-arg scaffolds. (n = 5 for each sample, *$p < 0.05$, **$p < 0.01$, and ***$p < 0.001$).

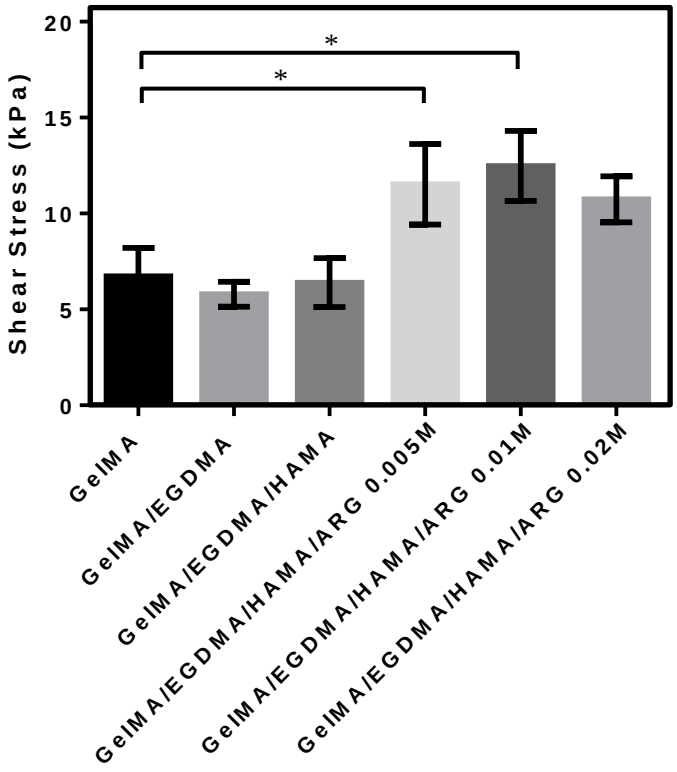

Figure 48. Quantification of maximum shear stress of electrospun GelMA/EGDMA/HAMA-arg scaffolds. (n = 5 for each sample, *p < 0.05).

Next, we assessed the adhesion strength and burst pressure of our artificial periosteum. An artificial periosteum needs to be applied without external aid to adhere to the fracture site in order to serve its purpose of stabilizing the osseous components and preventing soft tissue ingrowth to facilitate endochondral bone repair. Thus, the periosteum must stay adhered to the surface of bone while resisting substantial fluid pressure coming from potential bleeding during the operation. From the burst pressure data, it is observed that the addition of L-arginine significantly enhanced the burst pressure of the periosteum owing to its adhesive nature. This has allowed the 10 mM group to reach maximum burst pressure of 154.44 ± 24.89 mmHg, which is higher than the normal systolic pressure of healthy adults (120 mmHg). This demonstrates that the periosteum group is able to resist detachment after application owing to the potential fluid flow or bleeding during bone surgeries. On the other hand, the addition of L-arginine to the scaffold nearly doubled the adhesive strength of pure GelMA scaffolds, which allows it to hold bone tissues in place and serve as a bandage for bone operations. Altogether, we have demonstrated the clinical relevance and physical practicality of our periosteum in a surgical setting.

4.2.3 Biocompatibility, osteogenesis, and angiogenesis assessment of periosteum scaffold

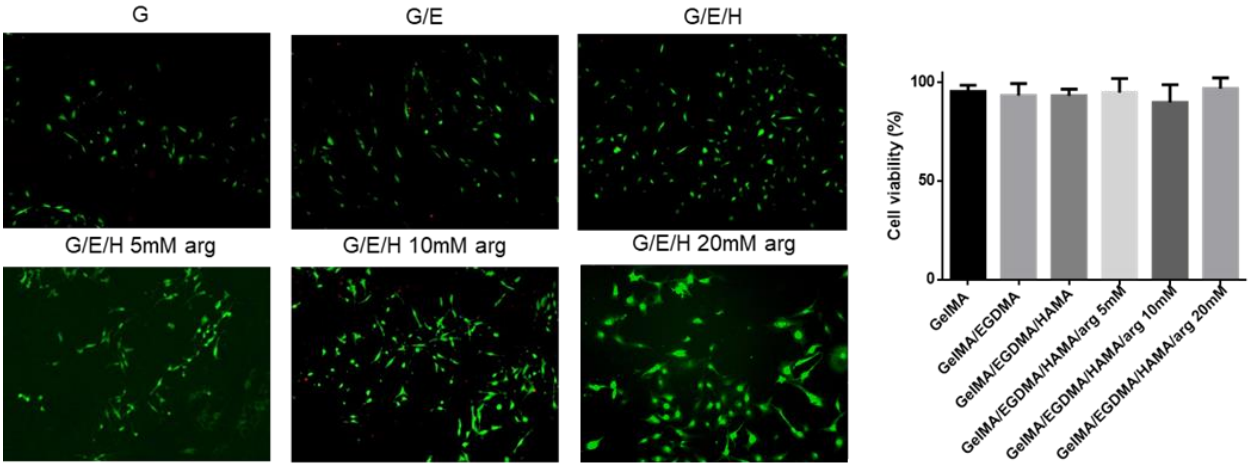

Figure 49. Live/Dead staining and quantification of MSCs seeded on various periosteum groups on day 1.

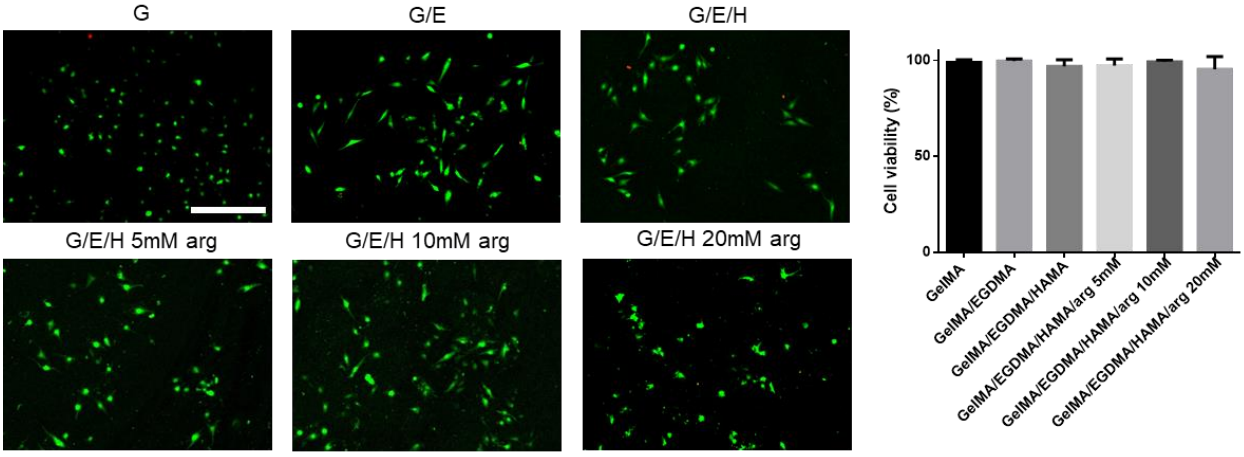

Figure 50. Live/Dead staining and quantification of HUVECs seeded on various periosteum groups on day 1.

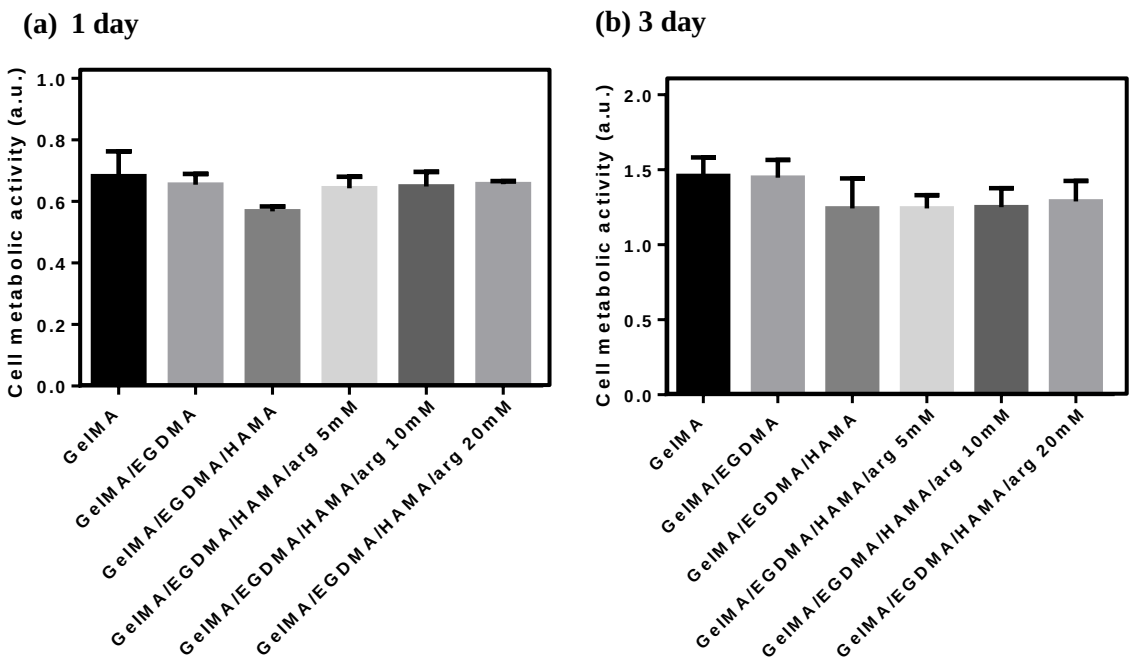

Figure 51. CCK-8 assay of MSCs seeded on periosteum groups after (a) 1 day and (b) 3 days (n = 4 for each sample, *p < 0.05).

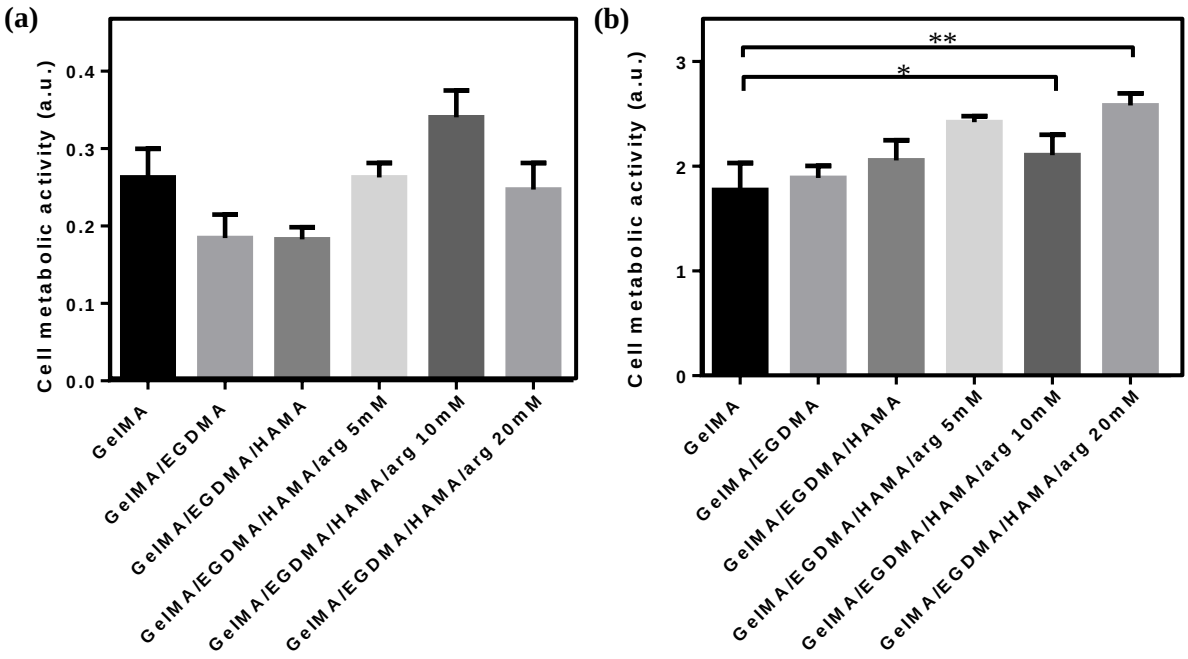

Figure 52. CCK-8 assay of HUVECs seeded on periosteum groups after (a) 1 day and (b) 3 days (n = 4 for each sample, *p < 0.05).

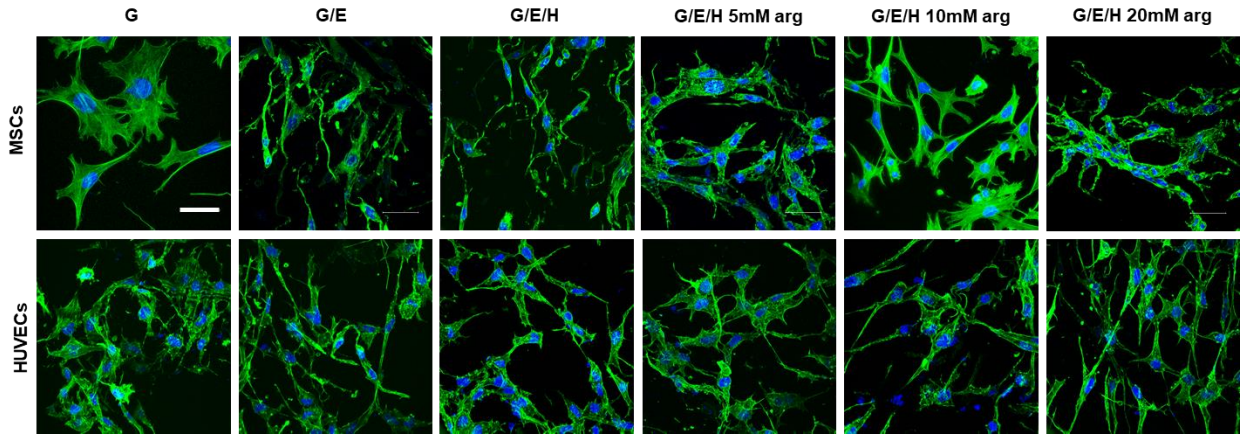

Figure 53. Actin/DAPI staining of MSCs and HUVECs seeded on periosteum groups (scale bar = 50 µm).

The ability to recruit native cells and support growth is of utmost importance for tissue repair. Thus, we first assessed the biocompatibility of our scaffolds. MSCs were chosen as a model cell for bone tissues while HUVECs were chosen for vascularized tissues. Both cell types on different periosteum groups displayed >95% viability, while the addition of L-arginine significantly increased the metabolic activity of HUVECs. To observe the morphology of cell adhesion on the membranes, phalloidin/DAPI staining was performed. Of note, both cell types displayed natural morphologies. HUVECs seeded on 20 mM arginine group, however, displayed signs of network formation and patterning, suggesting that the periosteum scaffold was able to induce changes in cell behaviour.

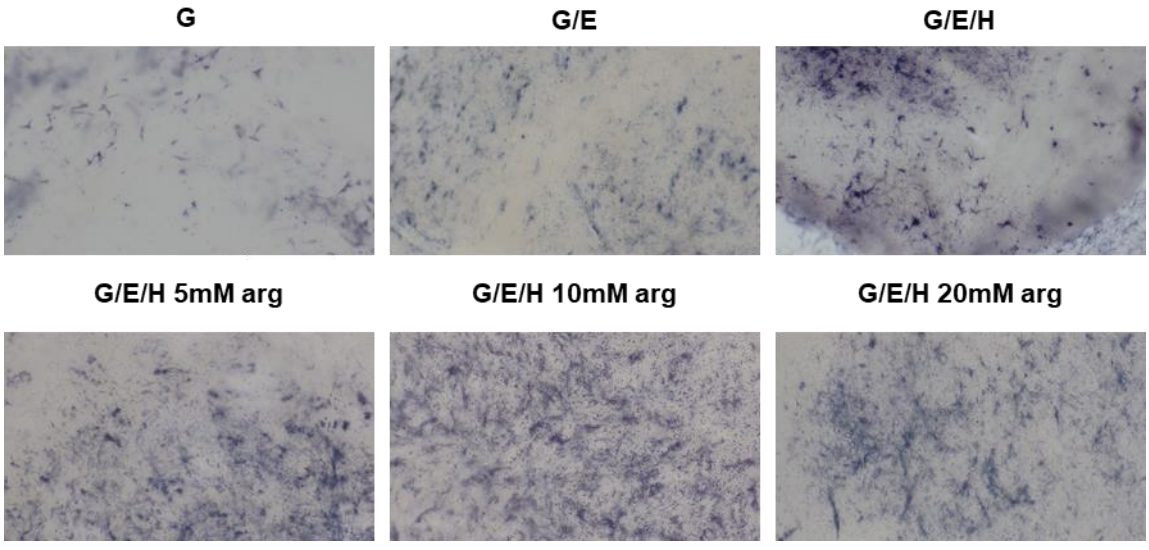

Figure 54. Alkaline Phosphatase Staining of MSC-seeded, osteogenic periosteum.

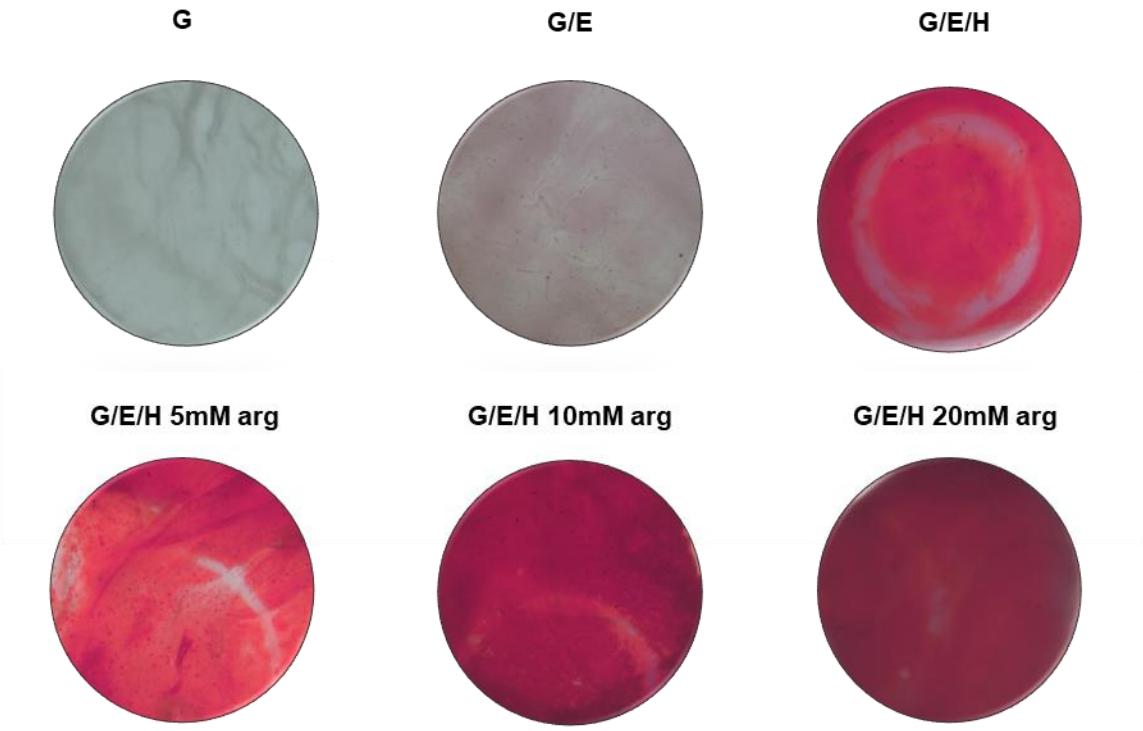

Figure 55. Alizarin Red S Straining of MSC-seeded, osteogenic periosteum.

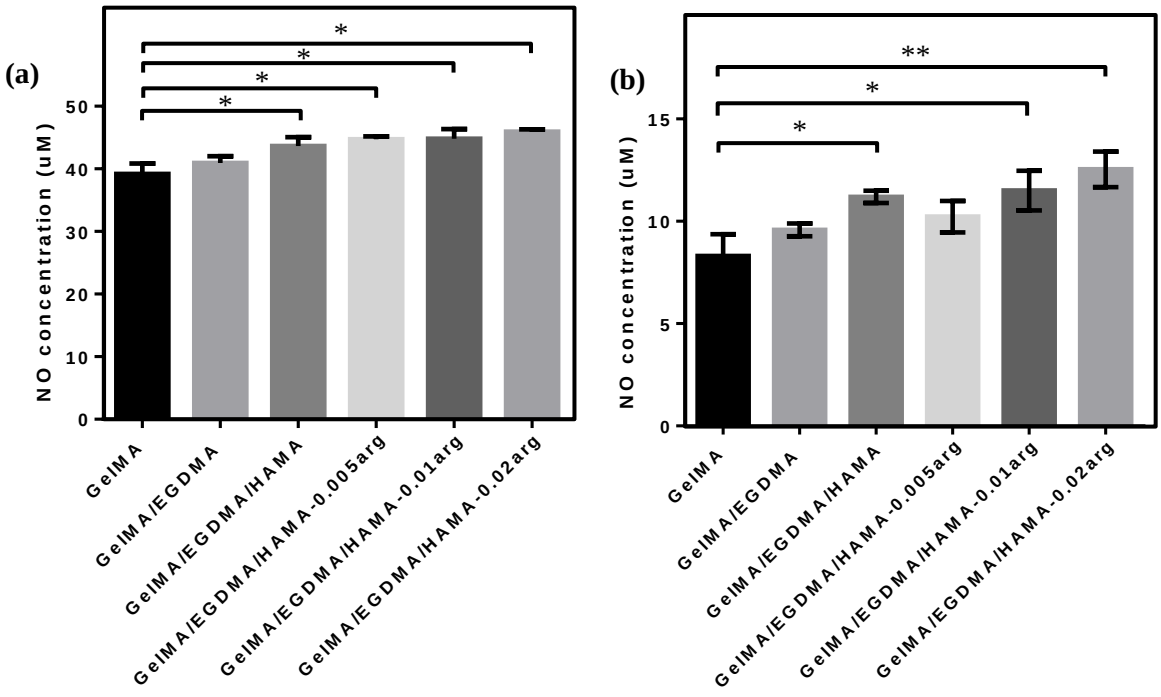

Figure 56. Nitric oxide generation of MSCs seeded on periosteum groups. (n = 5 for each sample, *p < 0.05, **p < 0.01)

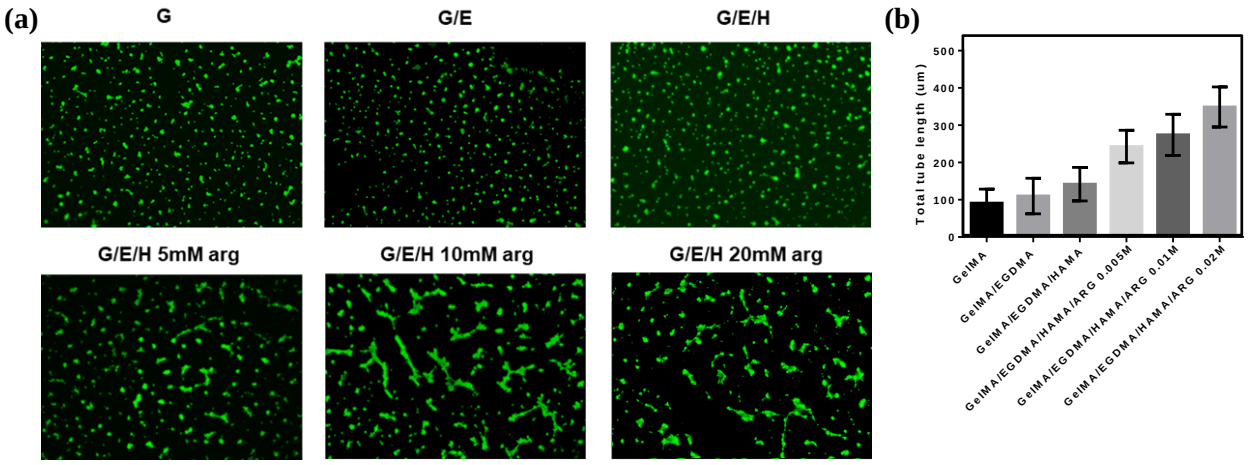

Figure 57. (a) Fluorescence image and (b) quantification of tube formation assay of HUVECs after 6 h of seeding on periosteum embedded Matrigel (scale bar = 100 μm).

Next, we moved onto assessment of osteogenesis and angiogenesis of our periosteum. For ALP stained samples, very low amounts of early osteogenesis is observed for pure GelMA samples, while there is a general increase in intensity for GelMA/EGDMA, GelMA/EGDMA/HAMA, and GelMA/EGDMA/HAMA-arg samples. The results for GelMA/EGDMA suggested that the increased mechanical property alone was able to contribute towards better osteogenic differentiation of MSCs into osteoblastic phenotypes, while the addition of HAMA and L-arginine progressively improved osteogenesis of MSCs. The same phenomenon is observed for ARS stained samples as abundance of stained cells could be observed on HAMA and L-arginine groups but not in pure GelMA or GelMA/EGDMA samples. This suggests that physical cues alone while can significantly improve osteogenesis, could not reach the same efficacy of supplementing the system with calcium ions and bioactive molecules which encourage osteogenic differentiation. This has been shown by many studies where MSCs were a primary paracrine for supporting endothelial formation and vessel cells, where molecules beneficial to angiogenic nature are able to favourably support proliferation and differentiation of osteogenic phenotypes simultaneously. This is reflected in the nitric oxide generation assay results, as both MSCs and HUVECs significantly increased in nitrite production when seeded on membranes with increased concentration of calcium ions and L-arginine. Additionally, membranes with varied L-arginine content showed dose-dependent relationship with HUVEC endothelial tube formation. With increasing L-arginine concentration, HUVECs demonstrated more tendency to form tube-like and network structures. These results suggest that the periosteum is successful at stimulating the osteogenic-angiogenic coupling in native cells, which are encouraging for further study (e.g., small animal study, Western Blot/qPCR quantification of signalling molecules).

5. Discussion

5.1 Limitations and clinical implications of electrospun skin scaffolds

The objective of functionalized wound dressings is to augment the existing capabilities of a scaffold to stem bleeding, protect the wounded areas, encourage regeneration and subsequently prevent scarring. Our scaffolds owing to the material choice and electrospun fibrous nature, is able to act as a more effective pathogenic barrier owing to the small pore size, and achieve improved adhesion of fibroblasts. The different formulas of the wound dressing possess a diverse range of mechanical properties (2-10 MPa), which could cover a relatively wide range of skin tissues (4.6-20 MPa), allowing it to act as an artificial skin in the long term to withstand tensile stress. The high integrity of the scaffolds, compared with other natural materials such as hyaluronic acid and cellulose, also enable the possibility of encapsulating therapeutics for long-term sustained release (>90 days). In this project, we have mediated the drug release using different brush lengths of PLA on pore surfaces of MSNs, and shown that the pore size can be quantifiably modulated through reaction time with free lactide molecules. The decreased pore size led to a prevention of burst release of anti-scarring agents from the particles, and overall decrease in drug diffusion speed. This combined with the lock-and-key mechanism of hydrophobic PLA brushes, allowed for highly concentrated reservoirs (50 mg/mL) while retaining low drug release dosages. This design is further protected by the aqueous core of core-sheath spinning where PLA was again used as a protective shell to delay water influx, doubly serving as a barrier to increase drug diffusion distance. This has allowed for a relatively biocompatible drug delivery reservoir system with low cytotoxicity that did not cause direct cell death or inhibit adhesion. However, such concentrated dosages of anti-scarring agents pose a potential threat owing to defects in the scaffolds and/or damage inflicted owing to accidents, which may trigger complex body responses when applied clinically. This is particularly concerning as at high MSN concentrations, fibroblasts began to exhibit decreased spindle phenotypes and reduced proliferation rate. Notably, the prohibitive effects of anti-scarring agents are inhibitive to wound healing processes, and are reflected in rabbit ear cutaneous wound models. Herein, for further clinical studies of this drug reservoir system, careful dosage control and calculations based on simulation need to be carried out. Nevertheless, the concept of our electrospun fibrous scaffold as a long-term drug encapsulation reservoir can be applied for various applications as most components of the system are interchangeable. The concept of a porous nanoparticle with hydrophobic polymer brush, aqueous/organic core-sheath electrospinning as well as the encapsulated therapeutic can all be tailored to fit specific niches such as tendon adhesion and tumour inhibition.

5.2 Limitations and future research direction of electrospun periosteum scaffolds

The typical limitations of clinical bone grafts are the lack of functioning periosteum to support regeneration and prevent soft tissue ingrowth. Normally, clinical procedures involved in bone grafting rely on screws and metal plates for fixture, which are typically extremely invasive and can damage bone tissues, or casts which are not precise in terms of stabilizing bones. Additionally, the lack of a physical barrier causes cells such as fibroblasts to migrate into the defect site and form soft calluses which hinder bone formation instead of cartilaginous tissues that eventually develop into bones. This creates a great demand for artificial periosteum or bone bandages specific to the surgical setting. Our periosteum in wet conditions has demonstrated up to 100 kPa tensile modulus and up to 150 mmHg burst pressure exceeding the normal systolic blood pressure of human vascular systems, which proves its applicability under clinical settings. Its components and degradation products including Ca^{2+} and L-arginine were all FDA-approved biomaterials, and beneficial to osteogenic-angiogenic coupling, which encourages MSCs to develop angiogenic phenotypes and HUVECs to form functional vasculature networks for the transportation of nutrients and cell recruitment. In our results, our periosteum successfully induced cell proliferation, adhesion, and stimulated both early and late osteogenesis in terms of calcium-dependant biomarkers. The improved NO generation of both MSCs and HUVECs were suggested to be beneficial to endothelialisation, which were reflected in the tube formation assay results of our membrane.

Figure 58. Photograph of bilayer design periosteum scaffold after lyophilization.

To further bolster the clinical relevancy of our periosteum, we plan on augmenting our periosteum design with a second inner layer of lyophilized hydrogel. As demonstrated by many studies, lyophilized hydrogel coatings can improve the interfacial intractability of biomaterial surfaces. By crosslinking our outer periosteum layer on top of pure GelMA hydrogels, a double layered fibrous/gelatinized scaffold can be formed. The structure can then be crosslinked to form a bilayered scaffold with a fibrous outer layer and a highly porous inner layer, which would then be reverted to its bioactive form after absorbing water. The fibrous outer layer favours cell adhesion and proliferation of osteoblasts with stronger mechanical properties for robust fixation of bone defects; while the porous inner layer favours vascularization and ingrowth of endothelial cells to form interacting networks of vessels. This design is expected to perform better under a clinical setting, and will be established before the commencement of animal studies.

6. Conclusion

In face of current limitations of electrospun scaffolds, we have fabricated functional scaffolds using electrospinning in terms of both physical and chemical augmentations. For the prevention of hypertrophic scarring, a lock-and-key core sheath structure demonstrated exceptional drug retention potential, and was effective at inhibiting scar formation for over 90 days without burst release of anti-scarring agents or severe cytotoxicity in both *in vitro* and *in vivo* settings. As artificial periosteum, the organic-inorganic inter-crosslinking of GelMA/EGDMA/HAMA-arg scaffolds were able to exhibit enhanced mechanical robustness, adhesion, as well as bioactivity in stimulation of osteogenesis and angiogenesis for both MSCs and HUVECs. However, moving forward, both studies will face challenges in the control of therapeutic dosage used for human bodies. More testing in particular in large animals and clinical trials will be required to further consolidate the clinical effectiveness of our drug delivery platforms.

List of publication produced from work

1. Mao, M., Bei, H. P., Lam, C. H., Chen, P., Wang, S., Chen, Y., ... & Zhao, X. (2020). Human-on-Leaf-Chip: A Biomimetic Vascular System Integrated with Chamber-Specific Organs. Small, 16(22), 2000546.
2. Bei, H. P., Hung, P. M., Yeung, H. L., Wang, S., & Zhao, X. (2021). Bone-a-Petite: Engineering Exosomes towards Bone, Osteochondral, and Cartilage Repair. Small, 2101741.
3. Pan, B. H., Zhang, Q., Lam, C. H., Yuen, H. Y., Kuang, S., & Zhao, X. (2021). Petite miracles: insight into the nano-management of scarless wound healing. Drug discovery today.
4. Yang, Y., Xu, T., Bei, H. P., Zhao, Y., & Zhao, X. (2021). Sculpting Bio-Inspired Surface Textures: An Adhesive Janus Periosteum. Advanced Functional Materials, 2104636.
5. Yang, Y., Xu, T., Zhang, Q., Piao, Y., Bei, H. P., & Zhao, X. (2021). Biomimetic, Stiff, and Adhesive Periosteum with Osteogenic–Angiogenic Coupling Effect for Bone Regeneration. Small, 17(14), 2006598.
6. Wang, W., Lu, L., Bei, H. P., Li, X., Du, Z., Maitz, M. F., ... & Yang, Z. (2021). Self-Protonating, plasma polymerized, superimposed multi-layered biomolecule nanoreservoir as blood-contacting surfaces. Chemical Engineering Journal, 410, 128313.
7. Rao, J., Pan Bei, H., Yang, Y., Liu, Y., Lin, H., & Zhao, X. (2020). Nitric oxide-producing cardiovascular stent coatings for prevention of thrombosis and restenosis. Frontiers in Bioengineering and Biotechnology, 8, 578.
8. Mei, Q., Rao, J., Bei, H. P., Liu, Y., & Zhao, X. (2021). 3D Bioprinting Photo-Crosslinkable Hydrogels for Bone and Cartilage Repair. International Journal of Bioprinting, 7(3).
9. Rao, J., Yang, Y., Bei, H. P., Tang, C. Y., & Zhao, X. (2020). Antibacterial nanosystems for cancer therapy. Biomaterials science, 8(24), 6814-6824.
10. Piao, Y., You, H., Xu, T., Bei, H. P., Piwko, I. Z., Kwan, Y. Y., & Zhao, X. (2021). Biomedical applications of gelatin methacryloyl hydrogels. Engineered Regeneration, 2, 47-56.

Reference

[1] S. Ramakrishna, An introduction to electrospinning and nanofibers, World Scientific2005.
[2] F. Higuera, Flow rate and electric current emitted by a Taylor cone, Journal of Fluid Mechanics 484 (2003) 303.
[3] V. Beachley, X. Wen, Effect of electrospinning parameters on the nanofiber diameter and length, Materials Science and Engineering: C 29 (2009) 663-668.
[4] Y. Kara, H. He, K. Molnár, Shear-aided high-throughput electrospinning: A needleless method with enhanced jet formation, Journal of Applied Polymer Science 137 (2020) 49104.
[5] C. Luo, M. Nangrejo, M. Edirisinghe, A novel method of selecting solvents for polymer electrospinning, Polymer 51 (2010) 1654-1662.
[6] B.-M. Min, G. Lee, S.H. Kim, Y.S. Nam, T.S. Lee, W.H. Park, Electrospinning of silk fibroin nanofibers and its effect on the adhesion and spreading of normal human keratinocytes and fibroblasts in vitro, Biomaterials 25 (2004) 1289-1297.
[7] F. Yang, R. Murugan, S. Wang, S. Ramakrishna, Electrospinning of nano/micro scale poly (L-lactic acid) aligned fibers and their potential in neural tissue engineering, Biomaterials 26 (2005) 2603-2610.
[8] J. Yoon, H.S. Yang, B.S. Lee, W.R. Yu, Recent progress in coaxial electrospinning: New parameters, various structures, and wide applications, Advanced Materials 30 (2018) 1704765.
[9] Y. Zhao, X. Zhu, H. Liu, Y. Luo, S. Wang, M. Shen, M. Zhu, X. Shi, Dendrimer-functionalized electrospun cellulose acetate nanofibers for targeted cancer cell capture applications, Journal of Materials Chemistry B 2 (2014) 7384-7393.
[10] X. Zhao, Z. Yuan, L. Yildirimer, J. Zhao, Z.Y. Lin, Z. Cao, G. Pan, W. Cui, Tumor-triggered controlled drug release from electrospun fibers using inorganic caps for inhibiting cancer relapse, Small 11 (2015) 4284-4291.
[11] G. Honari, Skin structure and function, Sensitive Skin Syndrome (2017) 26-32.
[12] A.L. Rippa, E.P. Kalabusheva, E.A. Vorotelyak, Regeneration of dermis: scarring and cells involved, Cells 8 (2019) 607.
[13] J.W. Penn, A.O. Grobbelaar, K.J. Rolfe, The role of the TGF-β family in wound healing, burns and scarring: a review, International journal of burns and trauma 2 (2012) 18.
[14] R. Ogawa, S. Akaishi, C. Huang, T. Dohi, M. Aoki, Y. Omori, S. Koike, K. Kobe, M. Akimoto, H. Hyakusoku, Clinical applications of basic research that shows reducing skin tension could prevent and treat abnormal scarring: the importance of fascial/subcutaneous tensile reduction sutures and flap surgery for keloid and hypertrophic scar reconstruction, Journal of Nippon Medical School 78 (2011) 68-76.
[15] G.G. Gauglitz, H.C. Korting, T. Pavicic, T. Ruzicka, M.G. Jeschke, Hypertrophic scarring and keloids: pathomechanisms and current and emerging treatment strategies, Molecular medicine 17 (2011) 113-125.
[16] J. Boateng, O. Catanzano, Advanced therapeutic dressings for effective wound healing—a review, Journal of pharmaceutical sciences 104 (2015) 3653-3680.
[17] M. Jannesari, J. Varshosaz, M. Morshed, M. Zamani, Composite poly (vinyl alcohol)/poly (vinyl acetate) electrospun nanofibrous mats as a novel wound dressing matrix for controlled release of drugs, International journal of nanomedicine 6 (2011) 993.
[18] H.-E. Thu, M.H. Zulfakar, S.-F. Ng, Alginate based bilayer hydrocolloid films as potential slow-release modern wound dressing, International journal of pharmaceutics 434 (2012) 375-383.

[19] J.H. Sung, M.-R. Hwang, J.O. Kim, J.H. Lee, Y.I. Kim, J.H. Kim, S.W. Chang, S.G. Jin, J.A. Kim, W.S. Lyoo, Gel characterisation and in vivo evaluation of minocycline-loaded wound dressing with enhanced wound healing using polyvinyl alcohol and chitosan, International journal of pharmaceutics 392 (2010) 232-240.
[20] A. Obermeier, J. Schneider, S. Wehner, F.D. Matl, M. Schieker, R. von Eisenhart-Rothe, A. Stemberger, R. Burgkart, Novel high efficient coatings for anti-microbial surgical sutures using chlorhexidine in fatty acid slow-release carrier systems, PloS one 9 (2014) e101426.
[21] C.M. Ryan, D.A. Schoenfeld, M. Malloy, J.T. Schulz, R.L. Sheridan, R.G. Tompkins, Use of Integra® artificial skin is associated with decreased length of stay for severely injured adult burn survivors, The Journal of burn care & rehabilitation 23 (2002) 311-317.
[22] F.E. Ahmed, B.S. Lalia, R. Hashaikeh, A review on electrospinning for membrane fabrication: challenges and applications, Desalination 356 (2015) 15-30.
[23] R. Augustine, E.A. Dominic, I. Reju, B. Kaimal, N. Kalarikkal, S. Thomas, Electrospun poly (ε-caprolactone)-based skin substitutes: I n vivo evaluation of wound healing and the mechanism of cell proliferation, Journal of Biomedical Materials Research Part B: Applied Biomaterials 103 (2015) 1445-1454.
[24] C.-H. Yao, C.-Y. Lee, C.-H. Huang, Y.-S. Chen, K.-Y. Chen, Novel bilayer wound dressing based on electrospun gelatin/keratin nanofibrous mats for skin wound repair, Materials Science and Engineering: C 79 (2017) 533-540.
[25] H.S. Yoo, T.G. Kim, T.G. Park, Surface-functionalized electrospun nanofibers for tissue engineering and drug delivery, Advanced drug delivery reviews 61 (2009) 1033-1042.
[26] G. Jin, M.P. Prabhakaran, S. Ramakrishna, Photosensitive and biomimetic core–shell nanofibrous scaffolds as wound dressing, Photochemistry and photobiology 90 (2014) 673-681.
[27] Q. Wei, F. Xu, X. Xu, X. Geng, L. Ye, A. Zhang, Z. Feng, The multifunctional wound dressing with core–shell structured fibers prepared by coaxial electrospinning, Frontiers of Materials Science 10 (2016) 113-121.
[28] G. Jin, M.P. Prabhakaran, D. Kai, S. Ramakrishna, Controlled release of multiple epidermal induction factors through core–shell nanofibers for skin regeneration, European Journal of Pharmaceutics and Biopharmaceutics 85 (2013) 689-698.
[29] J. Zhang, C. Xiao, X. Zhang, Y. Lin, H. Yang, Y.S. Zhang, J. Ding, An oxidative stress-responsive electrospun polyester membrane capable of releasing anti-bacterial and anti-inflammatory agents for postoperative anti-adhesion, Journal of Controlled Release (2021).
[30] J.R. Dwek, The periosteum: what is it, where is it, and what mimics it in its absence?, Skeletal radiology 39 (2010) 319-323.
[31] A. Oryan, S. Monazzah, A. Bigham-Sadegh, Bone injury and fracture healing biology, Biomedical and environmental sciences 28 (2015) 57-71.
[32] Q. Wang, J. Xu, H. Jin, W. Zheng, X. Zhang, Y. Huang, Z. Qian, Artificial periosteum in bone defect repair—A review, Chinese Chemical Letters 28 (2017) 1801-1807.
[33] K.S. Houschyar, C. Tapking, M.R. Borrelli, D. Popp, D. Duscher, Z.N. Maan, M.P. Chelliah, J. Li, K. Harati, C. Wallner, Wnt pathway in bone repair and regeneration–what do we know so far, Frontiers in cell and developmental biology 6 (2019) 170.
[34] S.J. Wimalawansa, Nitric oxide and bone, Annals of the New York Academy of Sciences 1192 (2010) 391.
[35] F. Mónica, K. Bian, F. Murad, The Endothelium-Dependent Nitric Oxide–cGMP Pathway, Advances in Pharmacology 77 (2016) 1-27.

[36] M. Gong, C. Chi, J. Ye, M. Liao, W. Xie, C. Wu, R. Shi, L. Zhang, Icariin-loaded electrospun PCL/gelatin nanofiber membrane as potential artificial periosteum, Colloids and Surfaces B: Biointerfaces 170 (2018) 201-209.
[37] M. Gong, C. Huang, Y. Huang, G. Li, C. Chi, J. Ye, W. Xie, R. Shi, L. Zhang, Core-sheath micro/nano fiber membrane with antibacterial and osteogenic dual functions as biomimetic artificial periosteum for bone regeneration applications, Nanomedicine: Nanotechnology, Biology and Medicine 17 (2019) 124-136.
[38] R. Shi, J. Zhang, K. Niu, W. Li, N. Jiang, J. Li, Q. Yu, C. Wu, Electrospun artificial periosteum loaded with DFO contributes to osteogenesis via the TGF-β1/Smad2 pathway, Biomaterials Science 9 (2021) 2090-2102.
[39] B. Pant, M. Park, S.-J. Park, Drug delivery applications of core-sheath nanofibers prepared by coaxial electrospinning: a review, Pharmaceutics 11 (2019) 305.
[40] J. Sun, J. Shen, S. Chen, M.A. Cooper, H. Fu, D. Wu, Z. Yang, Nanofiller reinforced biodegradable PLA/PHA composites: Current status and future trends, Polymers 10 (2018) 505.
[41] I.S. Khattab, F. Bandarkar, M.A.A. Fakhree, A. Jouyban, Density, viscosity, and surface tension of water+ ethanol mixtures from 293 to 323K, Korean Journal of Chemical Engineering 29 (2012) 812-817.
[42] S. Niedermayer, V. Weiss, A. Herrmann, A. Schmidt, S. Datz, K. Müller, E. Wagner, T. Bein, C. Bräuchle, Multifunctional polymer-capped mesoporous silica nanoparticles for pH-responsive targeted drug delivery, Nanoscale 7 (2015) 7953-7964.
[43] T. Sasaki, The effects of basic fibroblast growth factor and doxorubicin on cultured human skin fibroblasts: relevance to wound healing, The Journal of dermatology 19 (1992) 664-666.
[44] K. Yue, G. Trujillo-de Santiago, M.M. Alvarez, A. Tamayol, N. Annabi, A. Khademhosseini, Synthesis, properties, and biomedical applications of gelatin methacryloyl (GelMA) hydrogels, Biomaterials 73 (2015) 254-271.
[45] S. Moncada, A. Higgs, The L-arginine-nitric oxide pathway, New England Journal of Medicine 329 (1993) 2002-2012.
[46] H. Kalyanaraman, N. Schall, R.B. Pilz, Nitric oxide and cyclic GMP functions in bone, Nitric Oxide 76 (2018) 62-70.
[47] J.R. Lancaster, Simulation of the diffusion and reaction of endogenously produced nitric oxide, Proceedings of the National Academy of Sciences 91 (1994) 8137-8141.
[48] C. Meng, Y. Cao, L. Sun, Y. Liu, G. Kang, W. Ma, J. Peng, K. Deng, L. Ma, H. Wei, Synthesis of cyclic graft polymeric prodrugs with heterogeneous grafts of hydrophilic OEG and reducibly conjugated CPT for controlled release, Biomaterials science 8 (2020) 4206-4215.
[49] Y. Yang, X. Yan, Y. Cui, Q. He, D. Li, A. Wang, J. Fei, J. Li, Preparation of polymer-coated mesoporous silica nanoparticles used for cellular imaging by a “graft-from” method, Journal of Materials Chemistry 18 (2008) 5731-5737.
[50] S.O. Han, J.H. Youk, K.D. Min, Y.O. Kang, W.H. Park, Electrospinning of cellulose acetate nanofibers using a mixed solvent of acetic acid/water: Effects of solvent composition on the fiber diameter, Materials Letters 62 (2008) 759-762.